Competing orders in a frustrated Heisenberg model on the Fisher lattice

Atanu Maity [1,2,*] Yasir Iqbal [3,†] and Saptarshi Mandal [1,2,‡]

[1]*Institute of Physics, Bhubaneswar 751005, Odisha, India*

[2]*Homi Bhabha National Institute, Mumbai 400 094, Maharashtra, India*

[3]*Department of Physics, Indian Institute Of Technology Madras, Chennai 600036, Tamil Nadu, India*

(Received 9 July 2020; revised 18 October 2020; accepted 11 November 2020; published 3 December 2020)

We investigate the Heisenberg model on a decorated square (Fisher) lattice in the presence of first-neighbor J_1, second-neighbor J_2, and third-neighbor J_3 exchange couplings, with antiferromagnetic J_1. The classical ground-state phase diagram obtained within a Luttinger-Tisza framework is spanned by two antiferromagnetically ordered phases, and an infinitely degenerate antiferromagnetic chain phase. Employing classical Monte Carlo simulations we show that thermal fluctuations fail to lift the degeneracy of the antiferromagnetic chain phase. Interestingly, the spin-wave spectrum of the Néel state displays three Dirac nodal loops out of which two are symmetry protected while for the antiferromagnetic chain phase we find symmetry-protected Dirac lines. Furthermore, we investigate the spin $S = \frac{1}{2}$ limit employing a bond operator formalism which captures the singlet-triplet dynamics, and find a rich ground-state phase diagram host to a variety of valence bond solid orders in addition to antiferromagnetically ordered phases.

DOI: 10.1103/PhysRevB.102.224404

I. INTRODUCTION

In Mott-Hubbard insulators, a reasonable description of the localized electron state at low temperatures is provided by the Heisenberg spin Hamiltonian [1]. In the presence of frustrated interactions, which could be geometric or parametric in origin, the determination of the ground state and low-energy physics of the Heisenberg model poses itself as a highly nontrivial problem. The principal motivation in the investigation of frustrated spin systems lies in the lure of finding either magnetically ordered ground states with intricate spin textures or highly correlated nonmagnetic phases such as spin liquids [2–6]. To this end, transition metal oxides have attracted much attention as they are found in nature with a rich diversity of geometrically frustrated lattice structures, displaying a wide spectrum of magnetic behaviors [7,8]. In particular, in one such family of manganese oxide compounds (MnO_2) such as $K_{1.5}(H_3O)_xMn_8O_{16}$, $Ba_{1.2}Mn_8O_{16}$, and α–MnO_2 [9–11], the Mn ions reside on the vertices of a geometrically frustrated network, namely, the hollandite lattice [9,12,13]. Experimental studies on these systems have unveiled the presence of a plethora of magnetic phases upon variation of temperature, magnetic field, and doping, which include an antiferromagnetic state [14], a ferromagnet, helimagnetic order [15,16], and spin-glass behavior.

In order to understand the origin of this diversity in magnetic behaviors it is helpful to disentangle the effects of magnetic frustration from those arising due to the presence of impurities. Recently, theoretical studies employing an Ising model on the hollandite lattice [17,18] successfully explained the origin of the antiferromagnetic ground state in the disorder-free system [19] as well as the doping-induced transition into a spin-glass state [20–22]. However, the Ising model studied in Ref. [17] cannot account for helimagnetic (and in general noncollinear) orders observed in $K_{1.5}(H_3O)_xMn_8O_{16}$ and $K_{0.15}MnO_2$ at low temperatures [15,16]. Experimental investigations on manganese compounds [23–25] have provided evidence that these systems have small magnetic anisotropies and are thus well described by a Heisenberg model. The zero-temperature ($T = 0$) classical magnetic phase diagram of the Heisenberg model on the hollandite lattice allowing for different signs and strengths of nearest-neighbor couplings was studied in Ref. [26].

The hollandite lattice can be viewed either as coupled two-dimensional triangular lattices stacked in the z direction or as decorated square lattices (called Fisher lattice) stacked in the y direction [26]. An understanding of the magnetic Hamiltonian on a lattice which is a two-dimensional projection of the original three-dimensional lattice often provides valuable insights into how magnetic order develops in the original three-dimensional model, and helps flesh out the structure of the (often intricate) spin configurations. In this regard, investigation of the magnetic phases in the kagome lattice as an insightful route towards understanding the complex magnetism in the pyrochlore lattice is noteworthy [27]. Herein, we adopt the route of understanding the magnetism of the hollandite lattice by viewing it as coupled Fisher lattices since the nontrivial mechanism of magnetic order in α-MnO_2 materials seems to arise due to the coupling in the y direction [13,18,26,28]. In this work, we carry out a detailed analysis of the magnetic phases present in the $T = 0$ classical phase diagram and investigate fluctuation effects beyond the classical limit via a spin-wave analysis and a bond-operator formalism for spin $S = \frac{1}{2}$.

We consider a minimal model on the Fisher lattice (see Fig. 1) such that J_1 couples the vertices of neighboring

*atanu.maity@iopb.res.in

†yiqbal@physics.iitm.ac.in

‡saptarshi@iopb.res.in

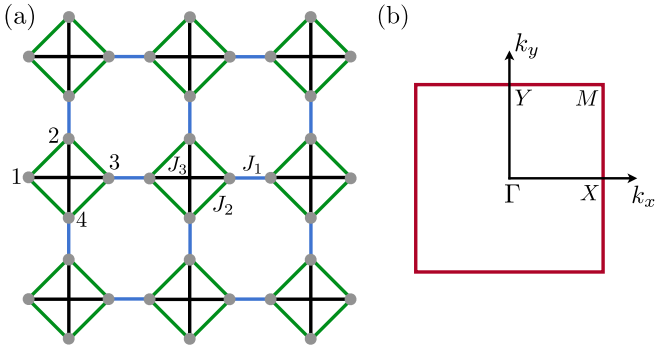

FIG. 1. (a) The Fisher lattice showing the three exchange couplings J_1 (blue) connecting sites on octagons, J_2 (green) connecting the sites of a square, and J_3 (black) connecting the diagonals of a square, of Eq. (1), with the four sites of the unit cell marked by 1, 2, 3, and 4. (b) The first Brillouin zone of the Fisher lattice with the high-symmetry points marked.

squares, J_2 defines the nearest-neighbor coupling within the squares, and J_3 is the second-nearest-neighbor (diagonal) coupling within each square. The inclusion of a J_3 coupling has been motivated from recent studies [13,28] which suggest that it might be necessary to describe the magnetism in hollandite systems. At the classical level, a Luttinger-Tisza analysis [29] of the (J_1, J_2, J_3) parameter space reveals the presence of different kinds of antiferromagnetically (AF) ordered states, an infinitely degenerate uncorrelated antiferromagnetic chain phase [30,31], as well as a unique Néel phase which features magnonic Dirac nodal lines depending on the sign and strength of the couplings. Furthermore, we investigate the role of quantum and thermal fluctuations on these ground states and find via (numerically) exact classical Monte Carlo simulations that thermal fluctuations fail to lift the degeneracy of the uncorrelated antiferromagnetic chain phase. We complement our study by going beyond the spin-wave approximation and compute the relative stability of the semiclassical ground state within a variational *Ansatz* by comparing the energies of competing states and find that each of them is stable as they feature a finite triplon excitation gap over suitable singlet states.

Our paper is structured as follows. In Sec. II, we define the model Hamiltonian and the Luttinger-Tisza framework employed to obtain the classical $T = 0$ phase diagram. In Sec. III A, we discuss the Luttinger-Tisza ground states and study the effect of thermal fluctuations employing classical Monte Carlo simulations. In Secs. IV and V, the impact of quantum fluctuations to harmonic order on the ground states is presented. In Sec. VI, we analyze our model Hamiltonian for spin $S = \frac{1}{2}$ within the scope of a bond-operator formalism and show the existence of three different types of quantum paramagnetic ground states, namely, a plaquette valence bond solid (VBS), and two other dimer ordered states. Finally, we summarize and discuss our results in Sec. VII.

II. MODEL AND METHODS

We consider a two-dimensional plane of the hollandite lattice [see Fig. 1(a)], called the decorated square (Fisher) lattice, which is characterized by a four-site geometrical unit cell.[1] The interactions between the spins localized on the vertices of this lattice are governed by a Heisenberg Hamiltonian

$$\hat{\mathcal{H}} = J_1 \sum_{\langle i,j\rangle_1} \hat{\mathbf{S}}_i \cdot \hat{\mathbf{S}}_j + J_2 \sum_{\langle i,j\rangle_2} \hat{\mathbf{S}}_i \cdot \hat{\mathbf{S}}_j + J_3 \sum_{\langle i,j\rangle_3} \hat{\mathbf{S}}_i \cdot \hat{\mathbf{S}}_j, \quad (1)$$

where the J_1, J_2, and J_3 superexchange couplings are schematically illustrated in Fig. 1(a). It is worth noting that in earlier studies [17,26] investigating the magnetism of the full three-dimensional hollandite lattice, the consideration of in-plane interactions was restricted to intersquare (J_1) and nearest-neighbor intrasquare (J_2) couplings only,[2] while the interplane coupling was found to yield helimagnetic order. Recent experimental studies [13,28] on hollandite compounds have pointed to relatively more intricate ground states compared to those found in Refs. [15–17,26]. In particular, in Ref. [28], the in-plane magnetic ground state was found to possess a magnetic unit cell which is a 4×4 expansion of the geometrical unit cell. Although the materials in question potentially involve more complex charge orderings which are likely to induce further magnetic coupling between the Mn atoms, it is understood that a simple model which accounts for only the above two mentioned in-plane interactions [J_1 and J_2 in Fig. 1(a)] is not sufficient to explain the formation of a magnetic order with a 4×4 magnetic unit cell. The above fact motivates us to explore a larger parameter space of exchange couplings, and to this end, we propose the simplest extension by introducing an additional second-nearest-neighbor (diagonal) coupling within each square, i.e., J_3 in Fig. 1(a). In our study we consider all possible signs and strengths of the (J_2, J_3) couplings with an antiferromagnetic J_1.

Our analysis of the ground states of the classical version of Eq. (1) employs the Luttinger-Tisza method. The corresponding classical model is obtained by normalizing the spin operators with respect to their angular momentum S and taking the limit $S \to \infty$ [32,33]. Consequently, the spin operators in Eq. (1) are replaced by ordinary vectors of unit length at each lattice site i. For a generic spin interaction, we have the following classical Hamiltonian that needs to be minimized:

$$\mathcal{H} = \sum_{i,j,\alpha,\beta} J_{\alpha\beta}(\mathbf{R}_{ij}) \mathbf{S}_{i,\alpha} \cdot \mathbf{S}_{j,\beta}, \quad (2)$$

where i, j denotes the corresponding Bravais lattice sites separated by lattice translation vectors $\mathbf{R}_{ij}$ and α, β indices denote the sublattice sites. The underlying Bravais lattice of the Fisher lattice is the square lattice. The Luttinger-Tisza method [29] seeks to find a ground state of Eq. (2) by enforcing the spin-length constraint at a global level, i.e., $\sum_i |\mathbf{S}_i^2| = S^2 N$, where N is the total number of lattice sites, a condition termed as the *weak constraint*. This constraint amounts to permitting

[1] In a hollandite lattice, the even and odd sublattices lie in different planes, but for the purposes of this study, this fact is not important.

[2] In Refs. [17,26] the J_1 and J_2 couplings in this paper are labeled as J_2 and J_3, respectively, while the interplane coupling is labeled as J_1. As we only deal with a given two-dimensional plane which is perpendicular to the channel directions, J_1 coupling of earlier studies is absent in our present analysis.

site-dependent average local moments which take us beyond the classical limit by approximately incorporating some aspects of quantum fluctuations [34].

A solution of this relaxed problem is achieved by decomposing the spin configuration into its Fourier modes $\tilde{\mathbf{S}}_\alpha(\mathbf{k})$ on the four sublattices of the Fisher lattice

$$\mathbf{S}_{i,\alpha} = \frac{1}{\sqrt{N/4}} \sum_{\mathbf{k}} \tilde{\mathbf{S}}_\alpha(\mathbf{k}) e^{\imath \mathbf{k}\cdot\mathbf{r}_{i,\alpha}}. \tag{3}$$

Inserting this expression into Eq. (2) results in

$$\mathcal{H} = \sum_{\mathbf{k}} \sum_{\alpha,\beta} \tilde{J}_{\alpha\beta}(\mathbf{k}) \tilde{\mathbf{S}}_\alpha(\mathbf{k}) \cdot \tilde{\mathbf{S}}_\beta(-\mathbf{k}), \tag{4}$$

with the interaction matrix given by

$$\tilde{J}_{\alpha\beta}(\mathbf{k}) = \sum_{i,j} J_{\alpha\beta}(\mathbf{R}_{ij}) e^{\imath \mathbf{k}\cdot\mathbf{R}_{ij}}. \tag{5}$$

$$\begin{pmatrix} 0 & J_2 e^{\imath(k_x-k_y)a} & J_3 e^{\imath 2k_x a} + J_1 e^{\imath k_x b} & J_2 e^{\imath(k_x+k_y)a} \\ J_2 e^{-\imath(k_x-k_y)a} & 0 & J_2 e^{\imath(k_x+k_y)a} & J_3 e^{\imath 2k_x a} + J_1 e^{\imath k_x b} \\ J_3 e^{-\imath 2k_x a} + J_1 e^{-\imath k_x b} & J_2 e^{-\imath(k_x+k_y)a} & 0 & J_2 e^{\imath(k_x-k_y)a} \\ J_2 e^{-\imath(k_x+k_y)a} & J_3 e^{-\imath 2k_x a} + J_1 e^{-\imath k_x b} & J_2 e^{-\imath(k_x-k_y)a} & 0 \end{pmatrix}.$$

In the region of parameter space defined by $J_3 > |J_2|$, we find that the minimal eigenvalue wave vector $(k_x, k_y)_0$ is given by

$$\begin{aligned} (k_x, k_y)_0 &= (2m\pi/3, k_y) \quad \text{or} \\ (k_x, k_y)_0 &= (k_x, 2n\pi/3), \end{aligned} \tag{6}$$

where $m, n \in \mathbb{Z}$, hence, realizing long-range ordering in one direction with an absence of relative ordering in the other direction. Along the line $J_2 = J_3$, we find

$$(k_x, k_y)_0 = (k_x, k_y), \tag{7}$$

leading to a degenerate ground-state manifold. In the remaining regions of parameter space we find

$$(k_x, k_y)_0 = ((2n+1)\pi/3, (2m+1)\pi/3), \tag{8}$$

which corresponds to long-range magnetic order with commensurate ordering wave vectors. The absence of an incommensurate ordering wave vector implies that the degree to which mutual interactions between spins are satisfied is likely to be determined locally and, hence, as a starting point it is helpful to pursue an energy minimization of a local cluster of spins. To this end, we employ a variational approach which proceeds by first constructing spin configurations of a local cluster of spins that minimize its energy and subsequently attempt to construct a global spin configuration which also satisfies the local minimum energy configuration of the cluster of spins. We verify the accuracy of our global spin configurations from classical Monte Carlo simulations.

To start with, we consider a cluster of four spins that constitute a unit cell of the Fisher lattice. The spin configuration is parametrized by observing that the lattice can be described as a collection of horizontal and vertical connections which are coupled via J_2 bonds. Each horizontal and vertical string of connections hosts two sublattices each. The relative orientation between the spins within both the sublattices is assigned an angle γ, while the relative orientation between the spins belonging to the same sublattice but in different chains is assigned an angle α [see Fig. 2(b)]. This choice of *Ansatz* gives an energy density

$$\begin{aligned} E/NS^2 = \tfrac{1}{4}(J_1[\cos(\gamma - k_x) + \cos(\gamma - k_y)] + J_2[2\cos\alpha \\ + \cos(\alpha+\gamma) + \cos(\alpha-\gamma)] + 2J_3\cos\gamma). \end{aligned} \tag{9}$$

The above expression has four free parameters which need to be determined to obtain the ground-state spin configuration. We note that since the antiferromagnetic J_1 bond is not frustrated by any other interaction, one may put forth an *Ansatz* in which the spins connected by the J_1 bonds are antiparallel, i.e., $k_x - \gamma = k_y - \gamma = \pi$, with Eq. (9) simplifying to

$$E/NS^2 = \tfrac{1}{2}[J_2\cos\alpha(1-\cos k_x) - J_3\cos k_x - J_1]. \tag{10}$$

Upon minimizing Eq. (10) with respect to k_x and α we get the following two sets of conditions for a spin configuration

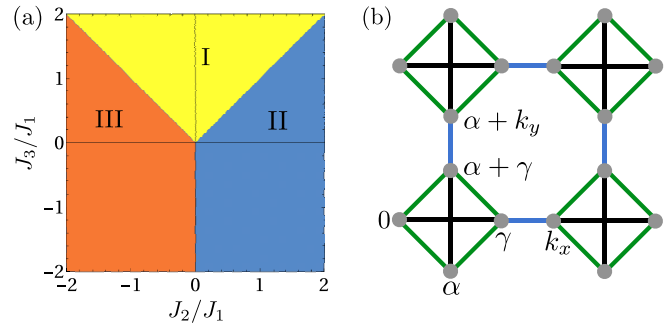

FIG. 2. (a) Classical phase diagram of J_1-J_2-J_3 Heisenberg model on the Fisher lattice with the couplings as defined in Fig. 1(a) and Eq. (1), (b) parametrization of a generic spin configuration with $\gamma = k_x + \pi$ and $k_x = k_y = k$.

III. CLASSICAL GROUND STATES

A. Luttinger-Tisza analysis

The interaction matrix $\tilde{J}_{\alpha\beta}(\mathbf{k})$ for our model takes the form

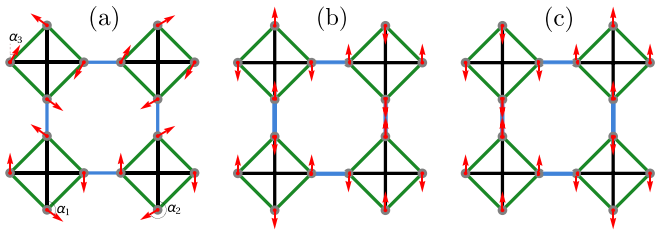

FIG. 3. Spin configuration in (a) phase I (uncorrelated antiferromagnetic chain) with $(k, \alpha) = (0, \alpha)$. The individual horizontal or vertical chains have perfect antiferromagnetic order, the relative orientations between them is not fixed. With respect to lower horizontal chain, the orientations of the two vertical chains are α_1 and α_2, respectively. Also, note that the orientation of upper horizontal chain with respect to lower horizontal chain is α_3, i.e., the system has an infinite degeneracy, (b) phase II (Néel phase) with $(k, \alpha) = (\pi, \pi)$, and (c) phase III (sublattice Néel phase) with $(k, \alpha) = (\pi, 0)$.

to qualify as a ground state:

$$\sin k_x(J_2 \cos\alpha + J_3) = 0, \tag{11}$$

$$\sin\alpha(1 - \cos k_x) = 0. \tag{12}$$

The solutions (k_x, α) satisfying the conditions [Eqs. (11) and (12)] corresponding to different phases are described below.

1. Antiferromagnetic chain phase

This phase is characterized by $(k, \alpha) = (0, \alpha)$ where $k = k_x = k_y$, and is stabilized for $J_3 \geqslant |J_2|$. It is depicted as phase I (yellow region) in the phase diagram of Fig. 2(a). It features perfect antiferromagnetic order along either the horizontal or vertical chains, however, there is a complete absence of spin correlations between any two of these ordered chains [see Fig. 3(a)]. This implies that within any given four-site unit cell, the spins coupled by J_3 bonds are antiferromagnetically correlated while there is no correlation between the spins connected by J_2. Hence, the angle α can take any value, implying an infinite degeneracy of the ground-state manifold. The ground-state energy is then independent of α:

$$E/NS^2 = -\tfrac{1}{2}(J_3 + J_1). \tag{13}$$

In the above expression, the independence of the energy on α arises due to a cancellation of the contributions from two bonds connected by J_2 within a given square plaquette. The existence of such a degeneracy within each square together with long-range antiferromagnetic order along horizontal or vertical chains poses itself as an interesting platform to investigate the order-by-disorder physics driven by thermal and quantum fluctuations. This will be discussed in Secs. III B, IV, and V.

2. Néel phase

For $J_3 < |J_2|$, we enter a region of parameter space where the arbitrariness in the choice of the parameter α in the uncorrelated antiferromagnetic chain phase gets lifted. In particular, for $J_2 > 0$ and $J_3 < J_2$, we obtain a Néel ordered phase [marked as phase II (blue region) in Fig. 2(a)]. This phase is characterized by $(k, \alpha) = (\pi, \pi)$ which signifies that within any given unit cell (square) there is perfect antiferromagnetic order, and that the spins in neighboring unit cells are aligned antiferromagnetically with respect to each other [see Fig. 3(b)]. However, unlike the familiar Néel phase on the square or honeycomb lattice, not all antiferromagnetic bonds are satisfied when $J_3 > 0$, as the spins connected by the J_3 couplings remain frustrated. The ground-state energy of this phase is given by

$$E/NS^2 = -\tfrac{1}{2}(2J_2 - J_3 + J_1). \tag{14}$$

Upon entering the region $J_3 < 0$, this phase is further stabilized since the spins coupled via J_3 bonds are ferromagnetically aligned in this Néel phase.

3. Sublattice Néel phase

In the region $J_2 < 0$, when $J_3 < |J_2|$, the free parameter α characterizing phase I is determined to zero implying that all spins within a given unit cell are ferromagnetically aligned. Furthermore, these four-site unit cells form Néel order throughout the lattice and, hence, each sublattice is Néel ordered [see Fig. 3(c)], we henceforth refer to this phase as a sublattice Néel ordered phase [marked as phase III (orange region) in Fig. 2(a)]. This state is thus characterized by $(k, \alpha) = (\pi, 0)$. The ground-state energy density can be written as

$$E = -\tfrac{1}{2}(2|J_2| - J_3 + J_1). \tag{15}$$

When $J_3 < 0$, the spin configuration satisfies all the couplings.

B. Classical Monte Carlo analysis

Since the Luttinger-Tisza approach is not *a priori* expected to give the exact ground-state spin configuration on a non-Bravais lattice such as ours, and given the fact that our approach is based on a variational *Ansatz* [Eq. (9)], we perform classical Monte Carlo simulations to investigate the accuracy of our analysis as well as to study the role of thermal fluctuations. It is worth mentioning that a two-dimensional system of Heisenberg spins with finite-range antiferromagnetic or ferromagnetic interactions cannot feature long-range order at any finite temperature by virtue of the Hohenberg-Mermin-Wagner theorem [37]. Our discussion thus refers to the behavior of order parameters (here spin orientations) at short length scales, i.e., at distances r less than the correlation radius ξ. We consider a system of 1600 $(= 20 \times 20 \times 4)$ spins, employ parallel tempering, and carry out simulations at temperatures $T/J_1S^2 = 0.001$.[3] We find that in phases II and III both the angles (γ, α) [see Fig. 2(b)] lock into the values $(0, \pi)$ and (0,0), respectively, as expected from the Luttinger-Tisza result. In contrast, in phase I, the angle γ settles into a value of π, while thermal order-by-disorder mechanism fails to lift the degeneracy in the angles α_1, α_2, and α_3 [see Fig. 3(a)] which therefore continue to exhibit a

[3]All the simulations have been performed starting from a high temperature of $T \sim J_1$ and reaching down until $T \sim 10^{-3}J_1$ through slow annealing. We have used 10^4 Monte Carlo steps for thermalization, followed by 10^5 Monte Carlo steps during which measurements are taken every 10 Monte Carlo steps to ensure uncorrelated results.

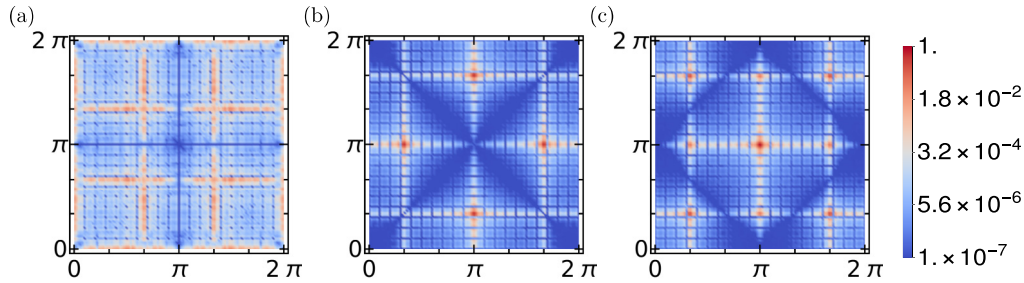

FIG. 4. The static (equal-time) spin structure factor obtained from classical Monte Carlo simulations for the three different phases in the classical phase diagram of Fig. 2(a) evaluated at $T/J_1S^2 = 0.001$ for a system of 1600 spins, (a) phase I at $(J_2/J_1, J_3/J_1) = (1, 4)$, (b) phase II at $(J_2/J_1, J_3/J_1) = (4, 1)$, and (c) phase III $(J_2/J_1, J_3/J_1) = (-4, 1)$.

fluctuating behavior with time evolution/Monte Carlo steps.[4] Furthermore, as the temperature $T \to 0$ the specific heat C tends to a value less than one, pointing to the important fact that the role of anharmonic fluctuation modes cannot be neglected. Our analysis thus provides evidence for the stabilization of an uncorrelated antiferromagnetic chain phase at *finite temperatures*. This is also reflected in the finding that within the region of parameter space occupied by phase I, the ground-state energy obtained from classical Monte Carlo simulations is independent of J_2 indicating an absence of spin correlations between the different horizontal and vertical chains. Hence, the spin configurations determined from the (numerically) exact classical Monte Carlo simulations are in complete agreement with those determined from the variational *Ansatz* [Eq. (9)], validating the classical phase diagram of Fig. 2(a).

Having discussed the classical ground states occupying the (J_1, J_2, J_3) parameter space, it is instructive to calculate the magnetic structure factor which can be experimentally measured in a neutron scattering experiment [38] to reveal the signatures of the magnetic ground states. As discussed above, we have found three different magnetic ground states, namely, an uncorrelated antiferromagnetic chain phase, Néel phase, and sublattice Néel phase, depending on the sign and magnitude of the exchange parameters in the Hamiltonian. Here, we calculate the static (equal-time) spin structure factor

$$S(\mathbf{k}) = \frac{1}{N}\sum_{i,j} e^{-\imath \mathbf{k}\cdot\mathbf{R}_{ij}} \langle \mathbf{S}_i \cdot \mathbf{S}_j \rangle \tag{16}$$

via classical Monte Carlo simulations for three different sets of parameter values. Here, N is the total number of sites, i and j run over all the sites of the lattice, and the nearest-neighbor distance between two sites is set to unity. This implies that the distance between the neighboring unit cells is three units which makes the periodicity of $S(\mathbf{k})$ as $2\pi/3$. In Fig. 4 we show the structure factor of the different phases in Fig. 2(a). We note that in phase I the horizontal and vertical chains are uncorrelated, and thereby have no global ordering in any direction, on average. The perfect antiferromagnetic order in a given chain yields a vanishing contribution when summed over all chains. Hence, we expect a featureless structure factor with the presence of subdued peaks at the zone boundary (corresponding to an ordering vector $\mathbf{k}$ which is zero upon a statistical averaging) as can be seen in Fig. 4(a). For the magnetic ground states given by phases II and III, we note that a global antiferromagnetic (Néel) order should yield peaks at $\mathbf{k} = (m\frac{\pi}{3}, n\frac{\pi}{3})$ where m, n are odd integers. However, the peaks at the above-mentioned points are modulated due to the form factor of the magnetic ordering in a given unit cell of Néel phase (phase II) and subattice Néel phase (phase III). These form factors lead to the appearance of blue lines along the diagonal for the phase II making a crosslike contour and for phase III a square pattern. The origin of such low intensity contours can be understood by calculating the structure factor for the Néel and the sublattice Néel phases analytically. An exact expression of the static structure factor for the different classical spin configurations obtained within a Luttinger-Tisza formalism (see Sec. III A) can be determined by evaluating Eq. (16) analytically. The static structure factor $\mathcal{F} = S^2|f|^2$ (where S denotes the form factor of the magnetization in a given unit cell and f arises due to global Néel ordering) thus obtained is given by

$$f = \frac{(1 - e^{\imath NLk_x})(1 - e^{\imath NLk_y})}{(4N)^2(1 + e^{\imath Lk_x})(1 + e^{\imath Lk_y})}, \quad L = 3a \tag{17}$$

$$S(\mathbf{k}) = 4(\cos k_x \mp \cos k_y)^2 \tag{18}$$

for a lattice of $N \times N$ unit cells, and $-$ $(+)$ corresponds to the form factor for the Néel (sublattice Néel) phase.

The form factor S is zero along the line $k_x = 2m'\pi \pm k_y$ for phase II and $k_x = (2m' + 1)\pi \pm k_y$ for phase III where m' is any integer including zero. Thus, the expected peaks at $\mathbf{k} = (m\frac{\pi}{3}, n\frac{\pi}{3})$ will be modulated due to such lines of zero intensity and it would remove some peaks in structure factor which are expected due to global Néel ordering. Figure 4(b) represents the structure factor for the Néel order (phase II). We see that the peaks appear at $\mathbf{k} = (m\frac{\pi}{3}, n\frac{\pi}{3})$ with $m \neq n$ due to the form factor modulation. On the other hand, such a

[4]We have verified the fluctuating behavior of the angles α_1, α_2, and α_3 down to temperatures $T \sim 10^{-5}J_1$. At low temperatures, we also perform a restricted Metropolis update: such an update proposes a new spin at random in a conical region about the local field of the old spin [85]. Adjusting the size of the conical region gives us control over the acceptance rate of proposed spins which is small at lower temperatures. In our simulation, the acceptance rate was around 50%. We have also checked the robustness of our findings by starting from an ordered state obtained by initializing the three angles to 0 and π and observing their evolution with Monte Carlo steps. The results are identical to those obtained by starting from a random configuration, namely, that they exhibit fluctuating behavior.

destructive modulation is absent for the sublattice Néel phase and the peaks appear at the expected locations $\mathbf{k} = (m\frac{\pi}{3}, n\frac{\pi}{3})$ with m and n being odd integers [see Fig. 4(c)]. In practice, a particular material may not have the exact symmetry of the lattice we have considered. For example, the unit cell may not be a square as taken here and also the distances between different sites of different neighbors connected by exchange couplings would also be different, in which case the experimentally obtained structure factor would be modified compared to that shown in Fig. 4. However, the structure factor in that case can be easily compared by evaluating Eq. (17) with modified lattice parameters, mainly the different values of $\mathbf{R}_{ij}$.

IV. SPIN-WAVE ANALYSIS

A. Antiferromagnetic chain phase

The $T = 0$ classical antiferromagnetic chain phase [phase I in Fig. 2(a)] has an infinitely degenerate ground-state manifold. In particular, on a lattice consisting of N horizontal and M vertical lines [see Fig. 2(b)], there are $N \times M$ independent α parameters, each of which can take on values ranging from 0 to 2π. It is thus natural to ask the question whether quantum fluctuations can lift this degeneracy via an order-by-disorder mechanism [39,40] and select a unique configuration parametrized by a certain value of α. To investigate the role of quantum fluctuations, we carry out a linear spin-wave analysis. To this effect, we rotate our coordinate system in such a way that the z axis of the local coordinate system coincides with the axis of the local spin orientation

$$\hat{S}_i^{\alpha} = R_x\left(\frac{\pi}{2}\right)R_z(\phi_i)\hat{S}_i^{\alpha'}, \quad \alpha = x, y, z. \tag{19}$$

The Holstein-Primakoff transformation [41] can now be written as

$$\begin{aligned}
\hat{S}_{i,m}^{z'} &\approx s - \hat{a}_{i,m}^{\dagger}\hat{a}_{i,m}, \\
\hat{S}_{i,m}^{x'} &\approx \sqrt{\frac{s}{2}}(\hat{a}_{i,m}^{\dagger} + \hat{a}_{i,m}), \\
\hat{S}_{i,m}^{y'} &\approx \imath\sqrt{\frac{s}{2}}(\hat{a}_{i,m}^{\dagger} - \hat{a}_{i,m}).
\end{aligned} \tag{20}$$

In the above $m = 1, 2, 3, 4$ denote the sublattice indices. Within a quadratic approximation to the boson operators we find that a uniform choice of α (when all $N \times M$ values of α are the same) is energetically favorable compared to disordered configurations of α (when all $N \times M$ values of α are different), indicating an order-by-disorder mechanism at work. This lifting of the degeneracy is only *partial* as α (which is now the same for all $N \times M$ sites) can still take on any value between 0 and 2π, yielding the same ground-state energy, and hence there still remain an infinite number of degenerate ground states. However, the magnon spectrum for each value of α need not be the same and thus we investigate the α dependence of the spin-wave spectrum. In Appendix A we provide the expressions of the resulting Hamiltonian after implementing the Holstein-Primakoff transformation corresponding to Eqs. (19) and (20). As expected, the Hamiltonian is invariant under $\mathcal{PT}$ symmetry which is defined as $\mathcal{PT} = \sigma_x \otimes \sigma_0\mathcal{K}$ (where $\mathcal{K}$ is the complex-conjugation operator). In phase I, the magnetic and crystallographic unit cells are identical, as a result of which we get a 8×8 Hamiltonian matrix [see Eq. (A1)] in $\mathbf{k}$ space. As a consequence of $\mathcal{PT}$ symmetry we obtain four doubly degenerate magnon branches shown in Fig. 5 with the following dispersion relations:

$$\epsilon(k)_{1,2} = \frac{1}{2}\sqrt{p_k \pm \frac{1}{2}\sqrt{Q(0)f_k + g_k(0) + h_k}}, \tag{21}$$

$$\epsilon(k)_{3,4} = \frac{1}{2}\sqrt{p_k \pm \frac{1}{2}\sqrt{Q(\alpha)f_k + g_k(\alpha) + h_k}}, \tag{22}$$

where $Q(\alpha) = \frac{2(J_2)^2\cos^2\alpha - (J_3)^2}{4}$ and

$$p_k = \frac{J_3}{4}(2 - \cos k_x - \cos k_y), \tag{23}$$

$$f_k = [\cos(k_x + k_y) + \cos(k_x - k_y)], \tag{24}$$

$$g_k(\alpha) = (J_2)^2\cos^2\alpha(1 - \cos k_x - \cos k_y), \tag{25}$$

$$h_k = (J_3)^2[2 + \cos(2k_x) + \cos(2k_y)]/8. \tag{26}$$

From Eq. (21) we see that there are two modes which are independent of α, and Eq. (22) shows that the other two modes are α dependent. For any given value of α there are two Goldstone modes originating from the spontaneously broken U(1) symmetry, and we observe the presence of zero-energy modes along the segments $\overline{\Gamma X}$ and $\overline{\Gamma Y}$. The presence of zero-energy modes can be understood from Eqs. (21) and (22) which upon substitution of $k_x(k_y) = 0$ and $k_y(k_x) = k$ yields $\epsilon(k) = 0$ and $\epsilon(k) = \sqrt{J_3}\sin k/2$. Hence, there are two doubly degenerate modes along the $k_x = 0$ and $k_y = 0$ axes out of which one doubly degenerate mode has zero excitation energy and another linearly dispersing in k for small values.

It is worth noting that along the $k_x = 0$ and $k_y = 0$ axes we have linear band crossings along the line segments $\overline{\Gamma X}$ and $\overline{\Gamma Y}$ in the Brillouin zone, thus forming Dirac nodal lines. We now discuss how the spin-wave spectrum depends on α. (i) For $\alpha = 0$ or π: in this case the system has two-sublattice Néel order. The Hamiltonian is block diagonal (see Appendix A), and each block is $\mathcal{PT}$ invariant which gives rise to two fourfold-degenerate bands [see Fig. 5(a)]. (ii) For $\alpha = \pi/4$: The block-diagonal structure disappears and as a result the two fourfold-degenerate bands split into four twofold-degenerate bands [see Fig. 5(b)]. (iii) For $\alpha = \pi/2$: In this case we have a band touching of the α-dependent bands at the M point which is a consequence of the underlying mirror reflection symmetry about the k_x, k_y, and $k_x = k_y$ axes. We note that there is a Dirac nodal line along the segment $\overline{\Gamma M}$ [see Fig. 5(c)]. Low-energy expansion of dispersion along $\overline{\Gamma M}$ gives

$$\epsilon(\kappa)_{1,2} = 2(J_3 \pm J_2\cos\alpha)|\sin\kappa/2|, \tag{27}$$

$$\epsilon(\kappa)_{3,4} = 2(J_3 \pm J_2)|\sin\kappa/2|. \tag{28}$$

In the above expressions, we have substituted $k_x = k_y = \kappa$. It is evident that the number of independent modes along the $\overline{\Gamma M}$ depends on α. For $\alpha = 0, \pi$ there are two doubly degenerate optical modes as represented by violet and blue lines in Fig. 5(a). When $\alpha = \pi/4$, the twofold degeneracy of both the optical modes gets lifted [see Fig. 5(b)], however,

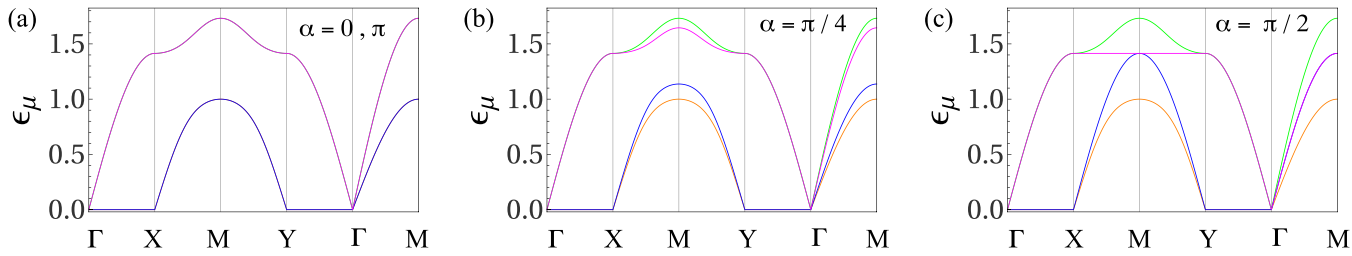

FIG. 5. Free magnon spectrum corresponding to Eqs. (21) and (22) in phase I for the parameter values $(J_2/J_1, J_3/J_1) = (1, 2)$ plotted along the high-symmetry path $\Gamma(0,0)$, $X(\pi,0)$, $M(\pi,\pi)$, and $Y(0,\pi)$ for three choices of degeneracy parameters, (a) $\alpha = 0$ or π, (b) $\alpha = \pi/4$ and (c) $\alpha = \pi/2$.

when $\alpha = \pi/2$ only the degeneracy of the lower optical mode gets lifted. The above observation may have experimental relevance in deciding the exchange parameter set for the model Hamiltonian or the selected angle α.

The appearance of doubly degenerate zero-energy modes along the $\overline{\Gamma Y}$ and $\overline{\Gamma X}$ is reminiscent of the fact that irrespective of the one-dimensional order along a certain direction, the perpendicular direction can adjust itself free of energy cost. We have also found that the inclusion of anisotropy or magnetic field perpendicular to the spin alignment plane leads to a lifting of the degeneracy of the optical modes along $\overline{YM}$ or $\overline{\Gamma M}$, however, the zero-energy mode along the $k_x(k_y) = 0$ survives on $\overline{\Gamma Y}$ and $\overline{\Gamma X}$ segments. The inclusion of higher-order terms may lift this degeneracy [42] but we expect the zero-energy modes at high-symmetry points to survive the inclusion of magnon-magnon interaction terms [43,44].

B. Phases II and III

This phase has perfect antiferromagnetic structure which is the same as for the unfrustrated case ($J_3 = 0$ and $J_1, J_2 > 0$) studied in Ref. [45] where the presence of two Dirac nodal loops was found. The magnetic unit cell (eight sites) is twice the size of the crystallographic unit cell (four sites). In the bipartite representation, the Hamiltonian can be written as in Eq. (A5), and is seen to be block diagonal with each block being $\mathcal{PT}$ invariant. This results in four fourfold-degenerate bands shown in Fig. 6. Similar to what was found for the unfrustrated model ($J_3 = 0$), we find two nodal loops [marked by blue line in Fig. 7(a)], namely, in Figs. 6(a) and 6(f) we see that the black circled points form one nodal loop while the cyan circled points form the second nodal loop. In the absence of a J_3 coupling it was shown in Ref. [45] that the Dirac nodal loops are topologically protected, and that there is a triple band touching at the Γ and M points, while in the presence of an additional J_3 coupling we find a quadruple band touching at the X and Y points as shown in Fig. 6(a). Furthermore, we find that a J_3 coupling leads to the appearance of an additional Dirac nodal loop along the Brillouin zone boundary and also along the $k_x(k_y) = 0$ axes [see Fig. 6(d) and the orange segment in Fig. 7(a)]. However, this additional loop appears only for particular choices of parameters shown in Fig. 7(b), and is not protected by any symmetry except at the time-reversal invariant momentum points, i.e., the Γ and M points [see Figs. 6(f) and 6(i)], where there remains a twofold degeneracy since the Hamiltonian given by Eq. (A5) is invariant under $\mathcal{T} = \imath\sigma_y\mathcal{K}$ operator.

In phase III, whose magnetic structure has an eight-site unit cell, we similarly find that the Hamiltonian (A8) is block diagonal with each block being $\mathcal{PT}$ invariant, leading to four fourfold-degenerate bands as in phase II. However, the symmetry-protected Dirac nodal loops of phase II are not found in phase III, on the other hand, the additional nodal loop along the zone boundary and $k_x(k_y) = 0$ axes found for phase II also appears in phase III for the same choice of parameters shown in Fig. 8. We note that the surface states for a ribbon geometry in phase II are gapless but the edge states for phase III are gapped.

V. THERMAL AND QUANTUM ORDER-BY-DISORDER EFFECTS

For a two-dimensional system of Heisenberg spins, the Hohenberg-Mermin-Wagner theorem dictates that even at infinitesimally small temperature, the deviation of the spin orientation, i.e., the spin fluctuations, is infinitely large. Thus, the assumption of small fluctuations about the classical ground state, i.e., the harmonic approximation is, in principle, not applicable. Nonetheless, the entropic selection of the dominant magnetic fluctuation tendencies at low temperatures carried out within a harmonic analysis may provide information on the nature of the short-range correlations. It is worth mentioning that the harmonic order results can be significantly altered if the anharmonic modes play a decisive role.

We now proceed to carry out such an analysis for phase I, which at zero temperature is infinitely degenerate being characterized any value of $\alpha \in [0, 2\pi)$. However, at finite temperature, the fluctuation of the spins explicitly contributes to the α-dependent free energy. This could possibly lead to a lifting of the degeneracy in the parameter α via a thermal order-by-disorder mechanism [46–48]. To this effect, we introduce a spin deviation $\theta_{\mathbf{R},\mu} \to {\theta^0}_{\mathbf{R},\mu} + \delta\theta_{\mathbf{R},\mu}$, where $\theta_{\mathbf{R},\mu}$ is the ground-state spin configuration of the μth sublattice of a unit cell with radius vector $\mathbf{R}$ and $\delta\theta_{\mathbf{R},\mu}$ is the deviation from ground-state spin configuration. Substituting this in Eq. (1) and expanding around the ground state up to quadratic order in $\delta\theta_{\mathbf{R},\mu}$, in Fourier space we obtain $\hat{\mathcal{H}} = E_{\rm GS} + \hat{\mathcal{H}}_{\rm fluctuation}$ with

$$\hat{\mathcal{H}}_{\rm fluctuation} = \sum_{\mathbf{q}} \psi^\dagger_{\mathbf{q}} A_{\mathbf{q}}(\alpha) \psi_{\mathbf{q}}, \tag{29}$$

where $\psi_{\mathbf{q}} = [\delta\theta_{\mathbf{q},1}\ \delta\theta_{\mathbf{q},2}\ \delta\theta_{\mathbf{q},3}\ \delta\theta_{\mathbf{q},4}]^T$, and $E_{\rm GS}$ is the ground-state energy.

In this (harmonic) approximation, the fluctuations can be integrated out in the partition sum, and give rise to a linear-T

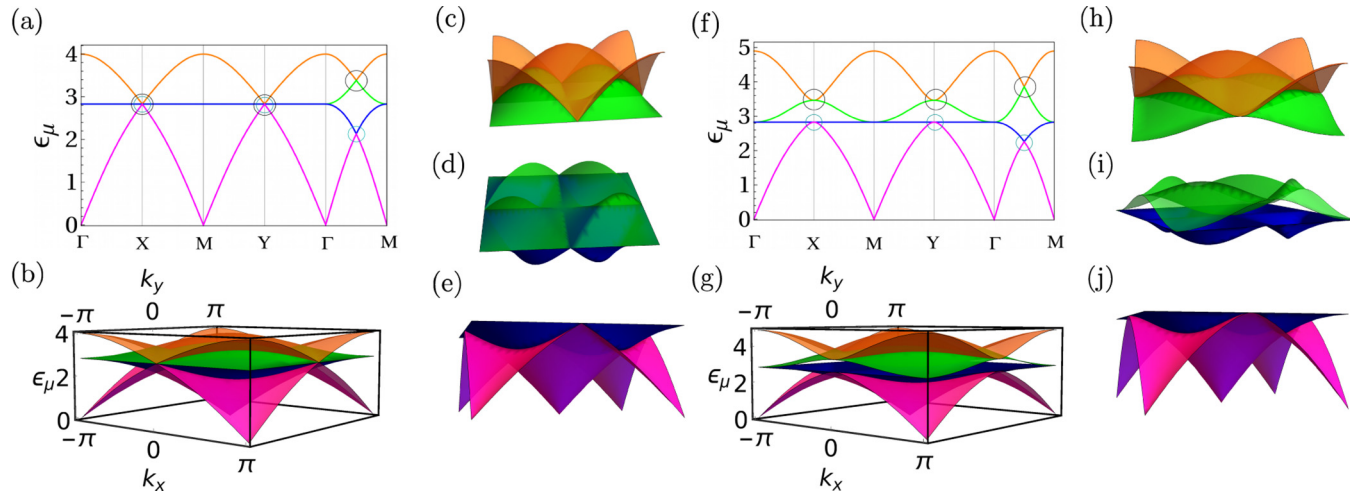

FIG. 6. Free magnon spectrum for phase II (Néel phase): (a), (b) $(J_2, J_3) = (2, 1)$ and (f), (g) $(J_2, J_3) = (3, 2)$, (c), (d), (e) and (h), (i), (j) represent the band touchings between different bands, which form the Dirac nodal loops for the two above-mentioned choices of parameters, respectively. Notice that the nodal loop due to touching of the bands denoted by green and blue colors appears for some choices of parameters and is gapped out for other choices. Hence, this nodal loop is not protected by any symmetry, whereas the nodal loops due to touching of the upper and lower two bands survive for all choices of parameters, thereby rendering these loops symmetry protected.

dependence in the free energy $\mathcal{F}(\alpha, T)$. Following Ref. [48], $\mathcal{F}(\alpha, T)$ can be written as

$$\mathcal{F}(\alpha, T) = E_{\rm GS} - NT \ln T + T \sum_{\mathbf{q}\in \rm BZ} \ln[\det A_{\mathbf{q}}(\alpha)], \quad (30)$$

where the last term is the α-dependent part of the low-temperature entropy density. The state which minimizes this term corresponds to the minimum of the free energy: this is the entropic order-by-disorder selection mechanism discussed in Refs. [39,40,47,48]. In the region of the phase diagram occupied by phase I, we find that thermal fluctuations select a value of α equal to 0 or π. This is in contrast to classical Monte Carlo result which finds that the order-by-disorder mechanism fails to lift the degeneracy in the angle α. Our results thus point to the non-negligible impact of anharmonic order fluctuations which seem to alter the harmonic order picture sharply in favor of an uncorrelated antiferromagnetic chain phase.

Furthermore, the energy of the spin-wave modes is $\hbar S \epsilon_{\mathbf{q},\mu}(\alpha)$ in the semiclassical description for spins of length $S \gg 1$. Quantum fluctuations then choose the state with the lowest zero-point energy

$$\mathcal{E}_{\rm ZP}(\alpha) = \sum_{\mathbf{q}\in \rm BZ} \frac{\hbar S}{2} \epsilon_{\mathbf{q},\mu}(\alpha). \quad (31)$$

The $\mathcal{E}_{\rm ZP}(\alpha)$ behaves qualitatively like the last term of Eq. (30) and selects the same ordering vectors. In the region of the phase diagram occupied by phase I, we find that at zero-temperature quantum fluctuations select a value of α equal to 0 or π. It will be interesting to investigate the impact of anharmonic order terms, which we leave for a future study.

VI. BOND-OPERATOR ANALYSIS: VALENCE BOND SOLID PHASES

In the extreme quantum limit of $S = \frac{1}{2}$, there arises the possibility of zero-point quantum fluctuations destroying long-range antiferromagnetic orders when the amplitude of the fluctuations becomes of the order of the spin length. Furthermore, the presence of frustrated interactions enhances quantum fluctuations, thereby aiding the stabilization of quantum paramagnetic phases such as quantum spin liquids and

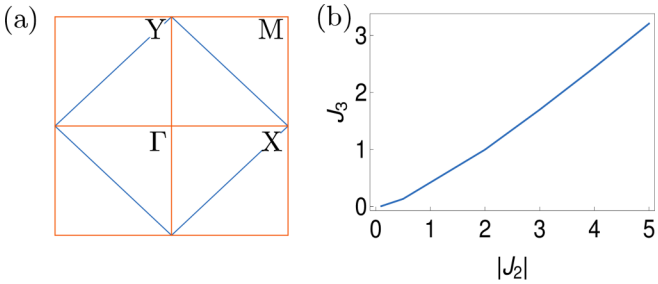

FIG. 7. (a) Projection of Dirac nodal loop on the first Brillouin zone. The blue line denotes the symmetry-protected nodal loops whereas the orange one appears for some specific choices of parameters. (b) Denotes the choices of parameters where the additional nodal loop appears which is not protected by any symmetry.

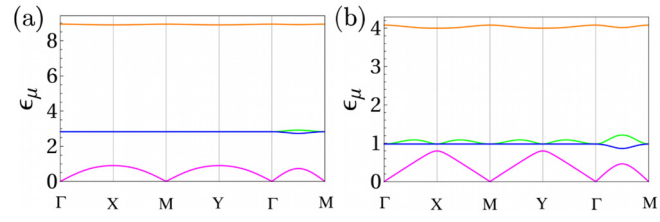

FIG. 8. Free magnon spectrum for phase III (sublattice Néel phase) for (a) $(J_2, J_3) = (-2, 1)$ and (b) $(J_2, J_3) = (-0.8, 0.6)$. Unlike Néel phase there is no robust Dirac nodal loop in this phase. However, similar to Néel phase in some choices of parameters a nodal loop (not protected by any symmetry) appears along the zone boundary and $k_x = 0$ and $k_y = 0$ axes as can be seen from (a).

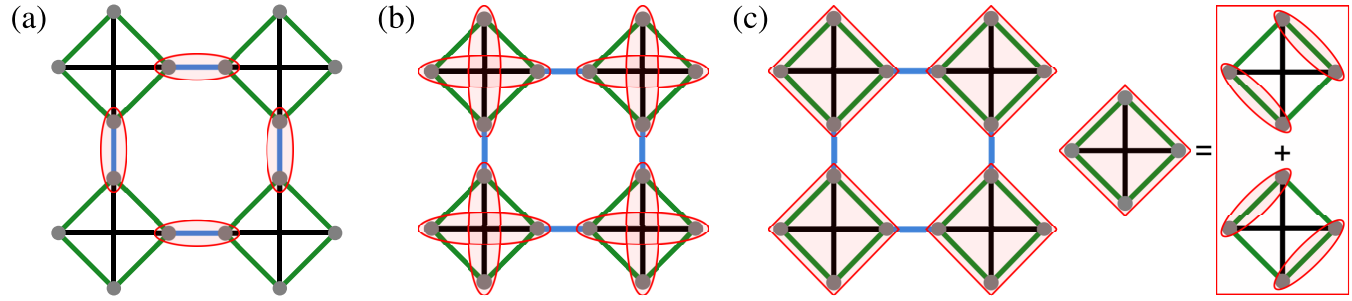

FIG. 9. A schematic illustration of the pattern of singlet dimer formations for the parameter regimes of Eq. (1), (a) $|J_1| \gg (|J_2|, |J_3|)$ (VBS_1), (b) $|J_3| \gg (|J_1|, |J_2|)$ (VBS_2), (c) $|J_2| \gg (|J_1|, |J_3|)$ (plaquette RVB) wherein the quantum ground state is given by a superposition of two states with dimer formation on the opposite sides of the square as shown in the right panel.

valence bond solids (VBS). Here, we investigate the effect of quantum fluctuations beyond the spin-wave approximation by employing resonating valence bond variational wave functions. We first investigate our J_1-J_2-J_3 model in parameter regimes where one of the couplings is overwhelmingly stronger compared to the remaining two. In this limiting regime, we note that at zeroth order the strongest bonds will form a singlet or triplet dimer and the locally excited states correspond to singlet-to-triplet excitations or *vice versa* for antiferromagnetic or ferromagnetic bonds, respectively (see Fig. 9). The effect of nonzero values of the remaining two (subdominant) couplings is to dynamically create local excitations on the strong singlet and triplet dimer bonds. Hence, an effective Hamiltonian of interacting singlet or triplet bonds between neighboring dimers can be constructed within this approach. This procedure is known to be effective in explaining the low-energy physics of interacting spin systems [49–57]. We now discuss the different VBS phases which are found to be realized as variational quantum ground states of the J_1-J_2-J_3 model.

A. VBS_1 and VBS_2 phases

In the limit when $|J_1| \gg (|J_2|, |J_3|)$ we have a VBS configuration consisting of dimers on J_1 type bonds [see Fig. 9(a)]. The local Hilbert space is four dimensional spanning the singlet ground state and the three triplets as the excited states. Following Ref. [51], we define $\hat{\psi}_i^\dagger$ and $\hat{\chi}_i^\dagger$ as the creation operators of the singlet and triplet states, respectively, on the ith bond within a given unit cell with the accompanying constraint on the dimensionality of the Hilbert space

$$\hat{\psi}_i^\dagger \hat{\psi}_i + \hat{\chi}_{i,\alpha}^\dagger \hat{\chi}_{i,\alpha} = 2S, \tag{32}$$

where $i = 1$ or 2 corresponds to the two J_1 type bonds in a unit cell, and $\alpha = 1, 2, 3$ denotes the three types of triplets in a given dimer. The interaction term between the two neighboring unit cells is obtained by writing the spin components in terms of the above-mentioned valence bond operators. This is achieved by calculating $\langle m|\hat{S}_\mu^\nu|n\rangle$ where $\mu = 1, 2$ denotes the two spins in a given dimer, $\nu = x, y, z$ labels the three spin components, and $|m\rangle$ ($|n\rangle$) represents the singlet or triplet states. In general, a spin operator at a given site has the form $\hat{S}_i \approx \frac{1}{2}(\hat{\psi}_i^\dagger \hat{\chi}_i + \text{H.c.})$ where i labels a given dimer (see Appendix B for details). As a result of this transformation we land up with a Hamiltonian which is quartic in the field operators $\hat{\chi}$ and $\hat{\psi}$. We carry out a mean-field decoupling such that the resulting quadratic Hamiltonian [Eq. (B2)] separates into singlet and triplet sectors with no mixing terms. The ground-state energy is obtained by extremizing the Hamiltonian with respect to the mean-field parameter N_i (where $\sqrt{N_i} = \langle\hat{\psi}_i^\dagger\rangle = \langle\hat{\psi}_i\rangle$) and the Lagrange multiplier λ needed to implement the constraint of Eq. (32), which yields two sets of self-consistent equations which are solved. The resulting expression for the ground-state energy per unit cell for VBS state in the parameter regime $J_1 \gg (J_2, J_3)$ is

$$\mathcal{E}_a = (N_{a,1} + N_{a,2})E_a - \lambda[(N_{a,1} + N_{a,2}) - 1] + \frac{3}{2N}\sum_{\mathbf{k}}\sum_{i=1}^{2}(\Theta_{\mathbf{k},i} - \mathcal{A}_{\mathbf{k},i}), \tag{33}$$

where a labels the VBS_1 state, $\Theta_{\mathbf{k},i}$ is the eigenenergy obtained in the triplon sector of the interacting Hamiltonian (B2) signifying the excitation of the triplet state [55], and $\mathcal{A}_{\mathbf{k},i}$ is the diagonal element of Eq. (B2). A similar procedure can be followed for the VBS_2 state in the parameter regime $J_3 \gg (J_1, J_2)$. For the VBS_2 state the unit cell has been conveniently chosen as an elementary square. In a similar manner as above, we obtain the ground-state energy per square

$$\mathcal{E}_b = (N_{b,1} + N_{b,2})E_b - \lambda[(N_{b,1} + N_{b,2}) - 1] + \frac{3}{2N}\sum_{\mathbf{k}}\sum_{i=1}^{2}(\Pi_{\mathbf{k},i} - \mathcal{B}_{\mathbf{k},i}), \tag{34}$$

where b labels the VBS_2 state, and the remaining terms all have identical meaning to that in Eq. (33) (see Appendix B for further details).

B. Plaquette VBS

In the parameter regime $(J_2, J_3) \gg J_1$ where we expect a plaquette VBS phase [see Fig. 9(c)], we have two choices of forming two dimers inside a square. More precisely, if we denote the four vertices of a square as V_1, V_2, V_3, and V_4, then we have two possibilities for dimer formation, namely, V_1-V_2 and V_3-V_4 or V_1-V_4 and V_2-V_3. The corresponding Hamiltonian is

$$\hat{\mathcal{H}}_p = J_2(\hat{\mathbf{S}}_1 + \hat{\mathbf{S}}_3)\cdot(\hat{\mathbf{S}}_2 + \hat{\mathbf{S}}_4) + J_3(\hat{\mathbf{S}}_1\cdot\hat{\mathbf{S}}_3 + \hat{\mathbf{S}}_2\cdot\hat{\mathbf{S}}_4). \tag{35}$$

The diagonalization of the above Hamiltonian gives the following two lowest-energy plaquette singlet states:

$$|\Psi_{p,(\pm)}\rangle = \frac{1}{\sqrt{2}}(|\psi_{1,2}\rangle|\psi_{3,4}\rangle \pm |\psi_{1,4}\rangle|\psi_{2,3}\rangle), \quad (36)$$

where $|\psi_{i,j}\rangle$ denotes a singlet state formed between the sites i and j, $|\Psi_{p,+}\rangle$ is the ground-state wave function with energy $E^s_+ = -2J_2 + \frac{J_3}{2}$ and $|\Psi_{p,-}\rangle$ is the first (singlet) excited state with energy $E_{s,-} = -\frac{3}{2}J_3$. Above these states lie the nine triplet states of the plaquette VBS with energies

$$E^t_{\mu,\mu} = \left(-J_2 + \frac{J_3}{2}\right)\delta_{\mu,3} - \frac{J_3}{2}(\delta_{\mu,1} + \delta_{\mu,2}), \quad (37)$$

where $\mu, \nu = 1, 2, 3$. The five quintet states have a degenerate energy $E_d = J_2 + \frac{J_3}{2}$. To capture the low-energy dynamics we have restricted our analysis to within the singlet-triplet manifold. The low-energy dynamics now includes, in addition to the triplet excited states considered for the VBS_1 and VBS_2 states, the singlet excited states. Within this approximation, the effective low-energy Hamiltonian for a single plaquette can be written as

$$\hat{\mathcal{H}}_p = \sum_{i=\pm} E_{s,i}\hat{\psi}^\dagger_{p,i}\hat{\psi}_{p,i} + \sum_{\mu,\nu=1}^{3} E_{t(\mu,\nu)}\hat{\chi}^\dagger_{(\mu,\nu)}\hat{\chi}_{(\mu,\nu)}. \quad (38)$$

Equations (35), (36), and (38) together with the constraint of Eq. (32) provide a complete description of the low-energy spectrum at zeroth order, i.e., in the absence of a J_1 interaction, leading to isolated plaquettes. The presence of a finite J_1 introduces interactions between neighboring plaquettes which induce transitions between different states of Eq. (38). The interplaquette interactions are obtained by writing the spin components in terms of the above-mentioned plaquette operators as was done for the VBS_1 and VBS_2 states (see Appendix C for details). The effective low-energy Hamiltonian for the interacting plaquette-VBS state thus obtained is given in Eq. (C3) (see Appendix C for details). The ground-state energy per plaquette is

$$\mathcal{E}_c = N_{c,+}(E_c - \lambda) + \lambda + \frac{3}{2N}\sum_{\mathbf{k}}\sum_{i=1}^{3}(\Omega_{\mathbf{k},i} - \mathcal{C}_{\mathbf{k},i}), \quad (39)$$

where $\sqrt{N_{c,+}} = \langle\hat{\psi}^\dagger_{p,+}\rangle = \langle\hat{\psi}_{p,+}\rangle$, $\Omega_{\mathbf{k},i}$ is the eigenenergy obtained in the triplon sector of the interacting plaquette Hamiltonian [Eq. (C3)].

Employing the expressions [Eqs. (33), (34) and (39)] of the ground-state energies of the three phases we map out the resulting phase diagram. The most salient feature of our phase diagram is the appearance of three quantum paramagnetic phases, namely, a plaquette VBS, and two other types of dimer ordered states dubbed VBS_1 and VBS_2 as shown in Fig. 10. The classical region of existence of the uncorrelated AF chain phase is now found to be divided into two regions under the influence quantum fluctuations. For $J_1 \gg (J_2, J_3)$, the VBS_1 state is stabilized while for $J_3 \gg (J_1, J_2)$, the VBS_2 state is stabilized. At the phase boundary of these two VBS states, a long-range ordered (LRO) state is found to be stabilized in a sliver of parameter space as inferred by the vanishing singlet-triplet excitation gap. We label this long-range ordered state as phase I (LRO) and it is characterized by the ordering

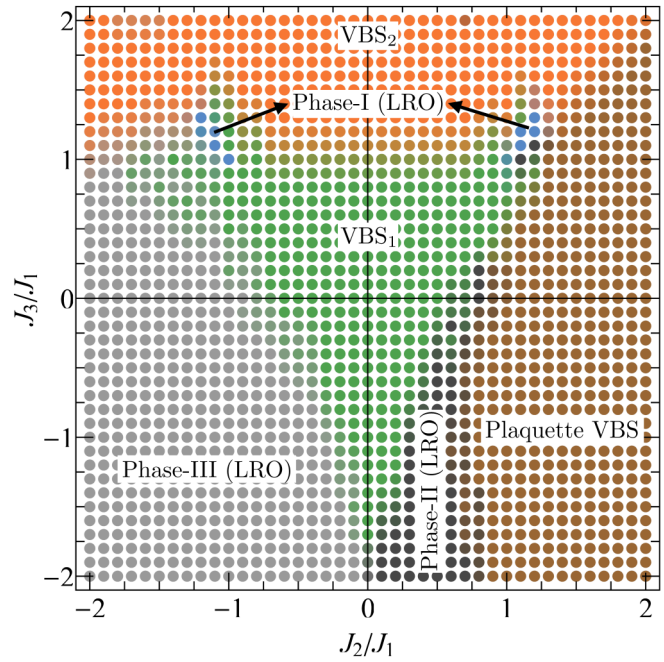

FIG. 10. Quantum phase diagram of the $S = \frac{1}{2}$ J_1-J_2-J_3 Heisenberg model on the Fisher lattice [Fig. 1(a)] obtained by a bond-operator analysis. We see the appearance of three different VBS phases in addition to the three long-range ordered (LRO) phases also present in the classical phase diagram [Fig. 2(a)].

vector $\mathbf{Q} = (0, k_y), (k_x, 0)$. The ordering wave vectors of the three LRO phases shown in Fig. 10 are determined by the momenta associated with the singlet-triplet gaps of the VBS phases that vanish at the Néel-VBS quantum phase transition.

Another interesting aspect of the quantum phase diagram is that the Néel phase [labeled as phase II in Fig. 2(a)] gives way to a plaquette-RVB state irrespective of the sign of the J_3 coupling. On the other hand, the sublattice Néel phase [labeled as phase III in Fig. 2(a)] is largely immune to quantum fluctuations, and is referred to as phase III (LRO) in Fig. 10. Apart from these phases, we find another long-range ordered phase in a small region for negative J_3 sandwiched between VBS_1 and plaquette VBS phases and label it as phase II (LRO) in Fig. 10. For the quantum paramagnetic phases such as VBS_1, VBS_2, and plaquette RVB, the singlet-triplet excitation gap is used as a measure of determining their stability as ground states with respect to inclusion of higher-order corrections. For the three long-range ordered phases shown in Fig. 10, the respective wave vectors which characterize these phases correspond to the vanishing of the singlet-triplet excitation gap of the VBS phases.

The singlet-triplet excitation gap for the various VBS phases is shown in Fig. 11. In Fig. 12, we present a density plot of the ground-state energy density for all the phases in the J_2-J_3 plane. It indicates that the ground-state energy of the LRO phases is higher compared to the VBS phases which highlights the role of quantum fluctuations in stabilizing quantum paramagnet phases. In Fig. 13, we present the excitation spectrum for different VBS phases at a few representative parameter values. In Figs. 13(a) and 13(b) we notice that depending on the value of J_3, the minimum of the dispersion

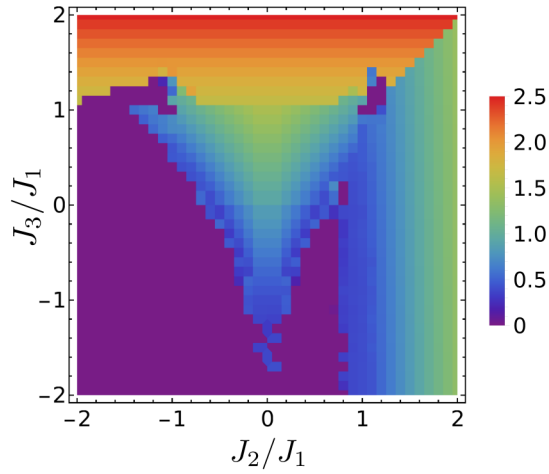

FIG. 11. Density plot of triplet excitation gap obtained by plaquette and bond-operator analysis.

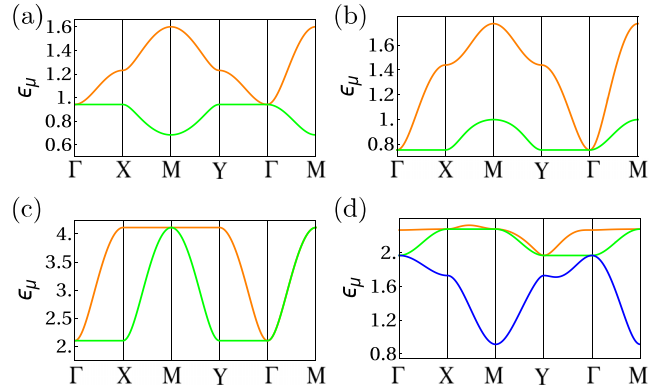

FIG. 13. Dispersion spectra for different VBS phases for representative values of $(J_2/J_1, J_3/J_1)$: (a) $\mathrm{VBS}_1(\pm 0.5, 0.3)$, (b) $\mathrm{VBS}_1(\pm 0.5, 0.7)$, (c) $\mathrm{VBS}_2(\pm 1.0, 1.5)$, and (d) plaquette VBS (1.5, 1.1).

occurs either at the M or the Γ point. The local minima at the M point changes to a local maxima upon increasing the value of J_3. This points to the fact that when $J_3 < J_2$ it is easier to create excitations through J_2 bonds which require an antiferromagnetic ordering between the dimers formed on J_1 bonds. This virtual antiferromagnetic ordering shows up as minima at the M points [see Fig. 13(a)]. However, when $J_3 > J_2$ such virtual antiferromagnetic ordering is not favorable as indicated by the local maxima at the M point [see Fig. 13(b)]. In Fig. 13(c) we present the excitation spectrum for VBS_2 which shows a maxima at the M point. The excitation spectrum for plaquette RVB shown in Fig. 13(d) is a gapped quadratic dispersion with minima at the M points.

The above results obtained within bond-operator formalism suggest that the large degeneracy in the disordered antiferromagnetic chain phase in the classical limit may not lead to a ground-state degeneracy in the exact quantum limit as indicated by the stability of the VBS_2 phase due to large values of the singlet-triplet excitation gap as shown in Fig. 11. On the other hand, the Néel phase which is known to be susceptible to quantum fluctuations gives way to a plaquette VBS state. It is to be noted that the singlet-triplet excitation gap for VBS_1 state is smaller compared to that of the VBS_2 state. In fact, Fig. 11 suggests that the singlet-triplet excitation gap gradually decreases with decreasing J_3. While the uncorrelated antiferromagnetic chain phase and Néel phase yield to quantum paramagnetic states under quantum fluctuations, remarkably the sublattice Néel phase is quite stable as evident from Fig. 10. This may be attributed to the fact that the number of nearest-neighbor bonds with ferromagnetic alignment is three times the number of bonds with antiferromagnetic alignment. The other possible explanation is that each square plaquette can be thought of as a large spin with magnitude of $4S$ which protects it from quantum fluctuations [58]. Finally, we note that similar observations of a plaquette VBS, and competing magnetic phases on a variant of the model, namely, the square kagome lattice Heisenberg model, have previously been made [59–64].

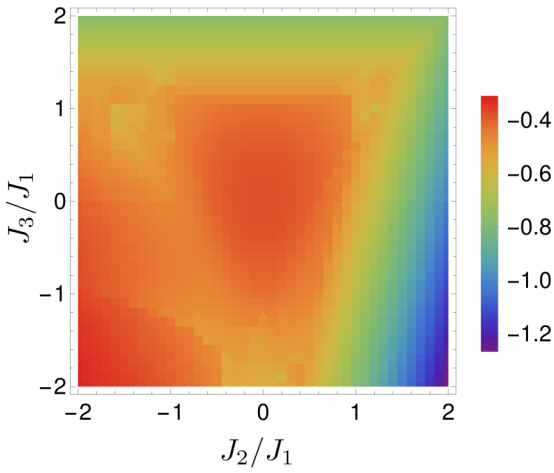

FIG. 12. Density plot of ground-state energy obtained by plaquette and bond-operator analysis.

VII. DISCUSSION

We have investigated the ground-state phase diagram of the Heisenberg model on the Fisher lattice in the presence of first-neighbor J_1, second-neighbor J_2, and third-neighbor J_3 Heisenberg couplings, as a route towards providing a magnetic model of a two-dimensional layer of the hollandite lattice. At the classical level, a Luttinger-Tisza analysis shows that the phase diagram is host to three different phases, namely, (i) an uncorrelated antiferromagnetic chain phase wherein each horizontal and vertical chain has perfect one-dimensional antiferromagnetic order, but the relative orientations between any two chains are not fixed at $T = 0$ [30,31,65]. This uncorrelated antiferromagnetic chain phase exists for $J_2 \geqslant J_3$ and antiferromagnetic J_2, J_3 *only*. Furthermore, there exist two different Néel phases depending on the sign of J_2. For antiferromagnetic J_2, we find a Néel phase (phase II) with the four spins within a unit cell being antiferromagnetically ordered. On the other hand, for ferromagnetic J_2, we find that the four spins within a unit cell are aligned ferromagnetically with such a cluster of ferromagnetic

spins forming Néel order, namely, the sublattice Néel order (phase III).

We have investigated the role of thermal and quantum order-by-disorder effects. Interestingly, our classical Monte Carlo analysis finds that the uncorrelated antiferromagnetic chain phase survives at finite temperature, i.e., the order-by-disorder mechanism fails to lift the degeneracy. On the other hand, a harmonic order analysis of quantum fluctuations reveals an order-by-disorder transition by selecting a common angle α between all the one-dimensional chains. We find that although the zeroth-order energy in the spin-wave approximation is identical for each α, the details of the spin-wave spectrum depend on the value of α, e.g., the spectrum could be linear or quadratic for different values of α, and the number of zero-energy modes depends on α. Interestingly, quantum fluctuations (within a harmonic order treatment) lift the degeneracy and select $\alpha = 0, \pi$. For specific choices of α, the spin-wave spectrum shows Dirac nodal lines along $\overline{\Gamma X}$ and $\overline{\Gamma Y}$ segments. The spin-wave spectrum for phase II reveals the presence of three Dirac nodal loops out of which two are symmetry protected and do not depend on the value of J_3.

Finally, we have employed a bond-operator formalism to analyze the model Hamiltonian beyond the spin-wave approximation. The analysis for spin $S = \frac{1}{2}$ shows that most of the classical phases except the sublattice Néel phase give way to different types of valence bond states. The region of parameter space classically occupied by the uncorrelated antiferromagnetic chain phase is stabilized into VBS_1 dimer order with an appreciable singlet-triplet excitations gap. This VBS_1 phase appears mostly for large positive values of J_3. In a triangular-shaped region around the center in the J_2-J_3 plane, a VBS_2 dimer state is stabilized. The Néel phase largely gives way to a plaquette VBS state, while the sublattice Néel phase is found to be stable under quantum fluctuations within the bond-operator formalism.

We expect that our study would set the stage for further investigations into the magnetic phases on the hollandite lattice [13,17,26,28]. The experimental realization of two-dimensional layers of α-MnO_2 (if possible) might serve as a platform to confirm the existence of some of the phases that have been found here. A possible extension of this study is to include a coupling between such two-dimensional layers yielding a three-dimensional model of magnetism in hollandite lattice. As a future endeavor, it would be interesting to study the spin $S = \frac{1}{2}$ quantum phase diagram employing state-of-the-art numerical quantum many-body frameworks such as pseudofermion functional renormalization group [66,67] and variational quantum Monte Carlo methods [68] which have already been applied on the square [69] and other two- and three-dimensional lattices [70,71]. In particular, for $S = \frac{1}{2}$ there exists the likely possibility of quantum spin liquid(s) occupying a finite region of parameter space [72]. It will be worthwhile to carry out a projective symmetry group classification [73] of U(1) and $\mathbb{Z}_2$ quantum spin liquids on the Fisher lattice. The resulting *Ansätze* and the competition between them could then be studied either by combining the projective symmetry group classification framework with a functional renormalization group approach [74] or employing variational Monte Carlo on the corresponding Gutzwiller projected wave functions supplemented by a few Lanczos steps [75–80]. In particular, it would be important to investigate their stability and energetic competitiveness with the valence bond solid orders, similar to what has been done on the kagome lattice [81,82]. Finally, we would like to mention that an interesting avenue for further exploration would be to possibly destabilize ferromagnetic order on the Fisher lattice, which could potentially give rise to a plethora of nematic orders as has been found in the square lattice [83,84].

ACKNOWLEDGMENTS

Y.I. thanks B. Dabholkar and K. Penc for helpful discussions. Y.I. acknowledges financial support by the Science and Engineering Research Board, Department of Science and Technology, Ministry of Science and Technology, India through the Startup Research Grant No. SRG/2019/000056 and MATRICS Grant No. MTR/2019/001042. This research was supported in part by the National Science Foundation under Grant No. NSF PHY-1748958, the Abdus Salam International Centre for Theoretical Physics (ICTP) through the Simons Associateship scheme funded by the Simons Foundation, the International Centre for Theoretical Sciences (ICTS), Bengaluru, India, during a visit for participating in the program Novel phases of quantum matter (Code: ICTS/topmatter2019/12) and the 2nd Asia Pacific Workshop on Quantum Magnetism (Code: ICTS/apfm2018/11). The Monte Carlo simulations were performed at SAMKHYA: High Performance Computing Facility provided by Institute of Physics, Bhubaneswar.

APPENDIX A: HAMILTONIAN FOR SPIN-WAVE SPECTRUM

In this Appendix, we explicitly write the Hamiltonian which is used to find the spectrum of spin-wave excitations.

1. Phase I

For phase I, which we refer to as the uncorrelated antiferromagnetic chain phase, the Hamiltonian matrix is

$$H_{\mathbf{k}} = \begin{bmatrix} A(\mathbf{k}) & B(\mathbf{k}) \\ B(\mathbf{k}) & A(\mathbf{k}) \end{bmatrix}. \tag{A1}$$

The basis vector is chosen to be $\hat{\tilde{\chi}}_{\mathbf{k}} = [\hat{\chi}_{\mathbf{k}}, \hat{\chi}^{\dagger}_{-\mathbf{k}}]^T$, with $\hat{\chi}_{\mathbf{k}} = (\hat{a}_{\mathbf{k},1}, \hat{a}_{\mathbf{k},2}, \hat{a}_{\mathbf{k},3}, \hat{a}_{\mathbf{k},4})$. In the above, $A_{\mathbf{k}}$ and $B_{\mathbf{k}}$ are 4×4 matrices

$$A_{\mathbf{k}} = \begin{bmatrix} a & b & 0 & -c \\ b & a & -c & 0 \\ 0 & -c & a & b \\ -c & 0 & b & a \end{bmatrix}, \tag{A2}$$

$$B_{\mathbf{k}} = \begin{bmatrix} 0 & c & b_x(\mathbf{k}) & -b \\ c & 0 & -b & b_y(\mathbf{k}) \\ b_x^*(\mathbf{k}) & -b & 0 & c \\ -b & b_y^*(\mathbf{k}) & c & 0 \end{bmatrix}. \tag{A3}$$

Among the various parameters that appear in the above two equations, a, b, c are constants with $a = \frac{1+J_3}{2}$, $b = \frac{J_2}{4}(1 - \cos\alpha)$, $c = \frac{J_2}{4}(1 + \cos\alpha)$. $b_{(x/y)}(\mathbf{k})$ is given below:

$$b_x(\mathbf{k}) = -\tfrac{1}{2}(J_3 + e^{\imath k_x}), \quad b_y(\mathbf{k}) = -\tfrac{1}{2}(J_3 + e^{-\imath k_y}). \tag{A4}$$

2. Phase II

For the Néel phase, the Hamiltonian becomes an 8×8 Hermitian matrix due to its four sublattice structure and the presence of global antiferromagnetic order. The basis vector which is used to define the Hamiltonian is $\hat{\tilde{\chi}}_{\mathbf{k}} = [\hat{\chi}_{\mathbf{k}}, \hat{\chi}^{\dagger}_{-\mathbf{k}}]^T$, with $\hat{\chi}_{\mathbf{k}}$=($\hat{a}_{\mathbf{k},1}$, $\hat{a}_{\mathbf{k},2}$, $\hat{a}_{\mathbf{k},3}$, $\hat{a}_{\mathbf{k},4}$, $\hat{b}^{\dagger}_{-\mathbf{k},1}$, $\hat{b}^{\dagger}_{-\mathbf{k},2}$, $\hat{b}^{\dagger}_{-\mathbf{k},3}$, $\hat{b}^{\dagger}_{-\mathbf{k},4}$), where $\hat{a}_{\mathbf{k}}$ and $\hat{b}_{\mathbf{k}}$, respectively, denotes the up spin and down spin in momentum space. The Hamiltonian is obtained as

$$H_{\mathbf{k}} = I_{2\times 2} \otimes \begin{bmatrix} A(\mathbf{k}) & B(\mathbf{k}) \\ B(\mathbf{k}) & A(\mathbf{k}) \end{bmatrix}, \tag{A5}$$

where $A_{\mathbf{k}}$ and $B_{\mathbf{k}}$ are given below:

$$A_{\mathbf{k}} = \begin{bmatrix} d & 0 & -J_3 & 0 \\ 0 & d & 0 & -J_3 \\ -J_3 & 0 & d & 0 \\ 0 & -J_3 & 0 & d \end{bmatrix}, \tag{A6}$$

$$B_{\mathbf{k}} = \begin{bmatrix} 0 & J_2 & e^{\imath k_x} & J_2 \\ J_2 & 0 & J_2 & e^{\imath k_x} \\ e^{-\imath k_x} & J_2 & 0 & J_2 \\ J_2 & e^{-\imath k_x} & J_2 & 0 \end{bmatrix}. \tag{A7}$$

In the above, $d = J_1 + 2J_2 - J_3$ and denotes the ground-state energy per plaquette in phase II.

3. Phase III

For the sublattice Néel phase, the basis vector used to define the Hamiltonian matrix for each momentum is identical to phase II. The Hamiltonian contains a few additional parameters. The Hamiltonian has the following expression:

$$H_{\mathbf{k}} = I_{2\times 2} \otimes \begin{bmatrix} A(\mathbf{k}) & B(\mathbf{k}) \\ B(\mathbf{k}) & A(\mathbf{k}) \end{bmatrix}, \tag{A8}$$

where $A_{\mathbf{k}}$ and $B_{\mathbf{k}}$ are given below:

$$A_{\mathbf{k}} = \begin{bmatrix} d & J_2 & -J_3 & J_2 \\ J_2 & d & J_2 & -J_3 \\ -J_3 & J_2 & d & J_2 \\ J_2 & -J_3 & J_2 & d \end{bmatrix}, \tag{A9}$$

$$B_{\mathbf{k}} = \begin{bmatrix} 0 & 0 & e^{\imath k_x} & 0 \\ 0 & 0 & 0 & e^{\imath k_x} \\ e^{-\imath k_x} & 0 & 0 & 0 \\ 0 & e^{-\imath k_x} & 0 & 0 \end{bmatrix}, \tag{A10}$$

where $d = J_1 - 2J_2 - J_3$ denotes the ground-state energy per plaquette in phase III.

APPENDIX B: VALENCE BOND-OPERATOR ANALYSIS

Here, we provide the detailed procedure followed in the bond-operator formalism. First, we give the definition of spins in terms of the fermionic field operators $\hat{\Psi}$ and $\hat{\chi}$ associated with the singlet and triplet excitations [51,55], respectively:

$$\hat{S}_{1,\alpha} \approx \tfrac{1}{2}(\hat{\chi}^{\dagger}_{\alpha}\hat{\psi} + \text{H.c.}), \quad \hat{S}_{2,\alpha} \approx -\tfrac{1}{2}(\hat{\chi}^{\dagger}_{\alpha}\hat{\psi} + \text{H.c.}). \tag{B1}$$

In the above, the subscripts 1, 2 refer to two spins within a dimer and $\alpha = x, y, z$ represents the three components of the spin. In defining the above transformation we have restricted ourselves up to quadratic order in the fields. The above definitions can be used to write the effective Hamiltonian in terms of the field operators. The effective Hamiltonian contains a Lagrangian multiplier λ in order to ensure that the magnitude of total spin of a given dimer is $2S$. It is straightforward to observe that the use of Eq. (B1) yields quartic terms in field operators. Mean-field type decomposition has been used to reduce these quartic terms into appropriate quadratic terms in singlet and triplet sectors, while neglecting the mixing between them. Furthermore, as we are interested in finding the excitations due to triplets over singlet condensation, we introduce $\sqrt{N_{a,i}} = \langle \hat{\psi}^{\dagger}_{a,i} \rangle = \langle \hat{\psi}_{a,i} \rangle$ as the singlet occupation number which is used to define the zeroth-order condensate energy $\tilde{E}_a$. Here, "a" denotes the VBS_1 configuration and "$i = 1, 2$" refers to two dimers within a unit cell. Similar definition holds for VBS_2 which is labeled by the subscript "b." Hence, we can write the effective Hamiltonian for the VBS_1 as

$$\hat{\mathcal{H}}_a = \tilde{E}_a + \frac{1}{2}\sum_{\mathbf{k}} \hat{\phi}^{\dagger}_{\mathbf{k},\alpha} H_{\mathbf{k},a} \hat{\phi}_{\mathbf{k},\alpha}. \tag{B2}$$

In the above expression, the singlet condensate energy $\tilde{E}_a$ is

$$\tilde{E}_{g,a} = (N_{a,1} + N_{a,2})E^s_a - \lambda(N_{a,1} + N_{a,2} - 1) - \frac{3}{2N}\sum_{\mathbf{k}}\sum_{i=1,2} A_{\mathbf{k},a,i}, \tag{B3}$$

where $A_{\mathbf{k},a,i}$ represents the ith diagonal element of $H_{\mathbf{k},a}$ and $E^s_a = -3J_1/4$ is energy of the singlet states per plaquette. The second term in Eq. (B2) refers to triplet excitations. The basis vector used to obtain Eq. (B2) is $\hat{\phi}_{\mathbf{k},\alpha} = [\hat{\xi}_{\mathbf{k}}, \hat{\xi}^{\dagger}_{-\mathbf{k}}]^T$, with $\hat{\xi}_{\mathbf{k}} = (\hat{\chi}_{a,1,\alpha,\mathbf{k}}, \ \hat{\chi}_{a,2,\alpha,\mathbf{k}})$, where α denotes different states within the triplet sector. It is clear that $H_{\mathbf{k},a}$ is a 4×4 matrix which can be written as

$$\hat{\mathcal{H}}_{\mathbf{k},a} = \begin{bmatrix} V_{\mathbf{k},a} + D_a & V_{\mathbf{k},a} \\ V_{\mathbf{k},a} & V_{\mathbf{k},a} + D_a \end{bmatrix}, \tag{B4}$$

where V and D are 2×2 matrices

$$V_{\mathbf{k},a} = \begin{bmatrix} -\frac{J_3}{2}N_{a1}\cos 2k_x & J_2 \sin k_x \sin k_y \\ J_2 N_{a12} \sin k_x \sin k_y & -\frac{J_3}{2}N_{a2}\cos 2k_y \end{bmatrix}, \tag{B5}$$

$$D_a = \begin{bmatrix} E^t_{a,\alpha} - \lambda & 0 \\ 0 & E^t_{a,\alpha} - \lambda \end{bmatrix}. \tag{B6}$$

In the above we have used $N_{a,12} = \sqrt{N_{a1}N_{a2}}$. E^t refers to energy of triplet states with $E^t_{a,\alpha} = J_1/4$, i.e., all the triplet states are degenerate in energy. To obtain the corresponding representations for VBS_2 we use the singlet- and triplet-state energies as $E^s_b = -3J_3/4$, $E^t_{b,\alpha} = J_3/4$. All other expressions of $V_{\mathbf{k},a}$ as given in Eq. (B4) will be replaced by $V_{\mathbf{k},b}$ which is given below:

$$V_{\mathbf{k},b} = \begin{bmatrix} -\frac{J_1}{2}N_{b1}\cos k_x & 0 \\ 0 & -\frac{J_1}{2}N_{b2}\cos k_y \end{bmatrix}. \tag{B7}$$

APPENDIX C: PLAQUETTE OPERATOR ANALYSIS

For the plaquette VBS state represented in Fig. 9(c), the spin operators are written as [50]

$$\hat{S}_{\delta,\alpha} \approx c_{\delta,\mu}(\hat{\chi}^{\dagger}_{\mu,\alpha}\hat{\psi}_{+} + \text{H.c.}) + d_{\delta,\nu}(\hat{\chi}^{\dagger}_{\mu,\alpha}\hat{\psi}_{-} + \text{H.c.}), \tag{C1}$$

where $\alpha = x, y, z$, $\mu = 1, 2, 3$ denotes the nine triplets, and $\delta = 1, 2, 3, 4$ denotes site indices inside a plaquette.

A summation over the repeated indices is implied in Eq. (C1). The matrices $c_{\delta,\mu}$ and $d_{\delta,\nu}$ are given as

$$c_{\delta,\mu} = \frac{1}{\sqrt{6}}\begin{bmatrix} \frac{1}{\sqrt{2}} & 0 & 1 \\ 0 & \frac{1}{\sqrt{2}} & -1 \\ -\frac{1}{\sqrt{2}} & 0 & 1 \\ 0 & -\frac{1}{\sqrt{2}} & -1 \end{bmatrix},$$

$$d_{\mu,\nu} = \frac{1}{2}\begin{bmatrix} 0 & 1 & 0 \\ 1 & 0 & 0 \\ 0 & -1 & 0 \\ -1 & 0 & 0 \end{bmatrix}. \tag{C2}$$

To derive the effective Hamiltonian as obtained for the valence bond singlet states in Appendix B in Eq. (B2), we follow a procedure similar to that explained before Eq. (B2). After doing elementary algebra we obtain the effective Hamiltonian in this case

$$\hat{\mathcal{H}}_c = \tilde{E}_c + \frac{1}{2}\sum_{\mathbf{k}} \hat{\phi}^{\dagger}_{\mathbf{k},\alpha} H_{\mathbf{k}} \hat{\phi}_{\mathbf{k},\alpha} + \sum_{\mathbf{k}} (E^s_- - \lambda)\hat{\psi}^{\dagger}_{\mathbf{k}-}\hat{\psi}_{\mathbf{k}-}. \tag{C3}$$

The first term $\tilde{E}_c$ in the above equation corresponds to ground-state condensate energy per plaquette. For the second term, we have used the basis vector as $\hat{\phi}_{\mathbf{k},\alpha} = [\hat{\xi}_{\mathbf{k}}, \hat{\xi}^{\dagger}_{-\mathbf{k}}]^T$, with $\hat{\xi}_{\mathbf{k}} = (\hat{\chi}_{1,\alpha,\mathbf{k}}, \hat{\chi}_{2,\alpha,\mathbf{k}}, \hat{\chi}_{3,\alpha,\mathbf{k}})$. Below we provide explicit expressions of the various terms present in Eq. (C3). First, we provide $\tilde{E}_c$,

$$\tilde{E}_c = N_{c+}E^s_+ - \lambda(N_{c+} - 1) - \frac{3}{2N}\sum_{\mathbf{k}}\sum_{i=1,2,3} \mathcal{C}_{\mathbf{k},i}, \tag{C4}$$

where we have used $\sqrt{N_{c+}} = \langle\hat{\psi}^{\dagger}_+\rangle = \langle\hat{\psi}_+\rangle$ and λ is the Lagrange multiplier to satisfy the constraint of total angular momentum of the dimer to be $2S$. $E^s_{\pm}$ is the plaquette singlet-state energy for the state $|\Psi_{\pm}\rangle$ with $E^s_+ = -2J_2 + \frac{J_3}{2}$, $E^s_- = -\frac{3J_3}{2}$. $\mathcal{C}_{\mathbf{k},i}$ is the ith diagonal element of $H_{\mathbf{k}}$. The 6×6 Hamiltonian matrix $H_{\mathbf{k}}$ in the second term of Eq. (C3) is

$$\hat{\mathcal{H}}_{\mathbf{k}} = \begin{bmatrix} W_{\mathbf{k}} + D_c & W_{\mathbf{k}} \\ W_{\mathbf{k}} & W_{\mathbf{k}} + D_c \end{bmatrix}, \tag{C5}$$

where

$$W_{\mathbf{k}} = \frac{N_{c+}}{3}\begin{bmatrix} \frac{-1}{2}\cos k_x & 0 & \frac{-\iota}{\sqrt{2}}\sin k_x \\ 0 & \frac{-1}{\sqrt{2}}\cos k_y & \frac{-\iota}{\sqrt{2}}\sin k_y \\ \frac{\iota}{\sqrt{2}}\sin k_x & \frac{\iota}{\sqrt{2}}\sin k_y & \cos k_x + \cos k_y \end{bmatrix}, \tag{C6}$$

$$D_c = \begin{bmatrix} E^t_{1,\alpha} - \lambda & 0 & 0 \\ 0 & E^t_{2,\alpha} - \lambda & 0 \\ 0 & 0 & E^t_{3,\alpha} - \lambda \end{bmatrix}, \tag{C7}$$

where $i, \alpha = 1, 2, 3$ denotes the nine triplet states. After diagonalization, the fluctuation due to triplon excitation contributes to the ground-state energy and the final expression for the ground-state energy can be written as given in Eq. (39). We note that the above analysis has been carried out for $J_2 > J_3$ where $|\Psi_+\rangle$ is the ground state and $|\Psi_-\rangle$ is the first excited state. When $J_3 > J_2$ with $J_1 = 0$, $|\Psi_-\rangle$ becomes the ground state and $|\Psi_+\rangle$ becomes the first excited state. Thus, there are parameter regimes where analogous analysis needs to be followed considering $|\Psi_-\rangle$ as the ground state. However, after doing that we find that the final energy obtained in the former case, i.e., when $|\Psi_+\rangle$ is the ground state, is lower compared to the case when $|\Psi_-\rangle$ is the ground state. To obtain the energy expression when $|\Psi_-\rangle$ is the ground state, one needs to replace the "$-$" subscript of the third term in Eq. (C3) by "+", "+" subscript in Eq. (C4) by "$-$". The expression of $W_{\mathbf{k}}$ as given in Eq. (C6) has the following form:

$$W_{\mathbf{k}} = \frac{-N_{c-}}{4}\begin{bmatrix} \cos k_y & 0 & 0 \\ 0 & \cos k_x & 0 \\ 0 & 0 & 0 \end{bmatrix}. \tag{C8}$$

[1] W. Heisenberg, Zur Theorie des Ferromagnetismus, Z. Phys. **49**, 619 (1928).

[2] I. Pomeranchuk, The thermal conductivity of the paramagnetic dielectrics at low temperatures, Zh. Eksp. Teor. Fiz. **11**, 226 (1941) [J. Phys. (USSR) **4**, 357 (1941)].

[3] L. Balents, Spin liquids in frustrated magnets, Nature (London) **464**, 199 (2010).

[4] L. Savary and L. Balents, Quantum spin liquids: A review, Rep. Prog. Phys. **80**, 016502 (2016).

[5] Y. Zhou, K. Kanoda, and T.-K. Ng, Quantum spin liquid states, Rev. Mod. Phys. **89**, 025003 (2017).

[6] C. Broholm, R. J. Cava, S. A. Kivelson, D. G. Nocera, M. R. Norman, and T. Senthil, Quantum spin liquids, Science **367**, eaay0668 (2020).

[7] C. N. R. Rao, Transition metal oxides, Annu. Rev. Phys. Chem **40**, 291 (1989).

[8] S. Maekawa, *Physics of Transition Metal Oxides* (Springer, Berlin, 1994).

[9] R. N. DeGuzman, Y.-F. Shen, E. J. Neth, S. L. Suib, C.-L. O'Young, S. Levine, and J. M. Newsam, Synthesis and characterization of octahedral molecular sieves (OMS-2) having the hollandite structure, Chem. Mater. **6**, 815 (1994).

[10] S. Ishiwata, J. W. G. Bos, Q. Huang, and R. J. Cava, Structure and magnetic properties of hollandite $Ba_{1.2}Mn_8O_{16}$, J. Phys.: Condens. Matter **18**, 3745 (2006).

[11] K. Hasegawa, M. Isobe, T. Yamauchi, H. Ueda, J.-I. Yamaura, H. Gotou, T. Yagi, H. Sato, and Y. Ueda, Discovery of Ferromagnetic-Half-Metal–to–Insulator Transition in $\mathbf{K_2Cr_8O_{16}}$, Phys. Rev. Lett. **103**, 146403 (2009).

[12] S. L. Suib and L. E. Iton, Magnetic studies of manganese oxide octahedral molecular sieves: A new class of spin glasses, Chem. Mater. **6**, 429 (1994).

[13] S. Liu, A. R. Akbashev, X. Yang, X. Liu, W. Li, L. Zhao, X. Li, A. Couzis, M.-G. Han, Y. Zhu, L. Krusin-Elbaum, J. Li, L. Huang, S. J. L. Billinge, J. E. Spanier, and S. O'Brien, Hollandites as a new class of multiferroics, Sci. Rep **4**, 6203 (2014).

[14] P. Strobel, J. Vicat, and D. T. Qui, Thermal and physical properties of hollandite-type $K_{1.3}Mn_8O_{16}$ and $(K,H_3O)_xMn_8O_{16}$, J. Solid State Chem. **55**, 67 (1984).

[15] H. Sato, J.-I. Yamaura, T. Enoki, and N. Yamamoto, Magnetism and electron transport phenomena of manganese oxide ion exchanger with tunnel structure, J. Alloys Compd. **262-263**, 443 (1997), proceedings of the Twelfth International Conference on Solid Compounds of Transition Elements.

[16] H. Sato, T. Enoki, J.-I. Yamaura, and N. Yamamoto, Charge localization and successive magnetic phase transitions of mixed-valence manganese oxides $K_{1.5}(H_3O)_xMn_8O_{16}(0 < x < 0.5)$, Phys. Rev. B **59**, 12836 (1999).

[17] Y. Crespo, A. Andreanov, and N. Seriani, Competing antiferromagnetic and spin-glass phases in a hollandite structure, Phys. Rev. B **88**, 014202 (2013).

[18] Y. Crespo and N. Seriani, Electronic and magnetic properties of α-MnO_2 from *ab initio* calculations, Phys. Rev. B **88**, 144428 (2013).

[19] N. Yamamoto, T. Endo, M. Shimada, and T. Takada, Single crystal growth of α-MnO_2, Jpn. J. Appl. Phys **13**, 723 (1974).

[20] X.-F. Shen, Y.-S. Ding, J. Liu, Z.-H. Han, J. I. Budnick, W. A. Hines, and S. L. Suib, A magnetic route to measure the average oxidation state of mixed-valent manganese in manganese oxide octahedral molecular sieves (OMS), J. Am. Chem. Soc. **127**, 6166 (2005).

[21] J. Luo, H. T. Zhu, F. Zhang, J. K. Liang, G. H. Rao, J. B. Li, and Z. M. Du, Spin-glasslike behavior of K^+-containing α-MnO_2 nanotubes, J. Appl. Phys. **105**, 093925 (2009).

[22] J. Luo, H. T. Zhu, J. K. Liang, G. H. Rao, J. B. Li, and Z. M. Du, Tuning magnetic properties of α-MnO_2 nanotubes by K^+ doping, J. Phys. Chem. C **114**, 8782 (2010).

[23] F. Moussa, M. Hennion, J. Rodriguez-Carvajal, H. Moudden, L. Pinsard, and A. Revcolevschi, Spin waves in the antiferromagnet perovskite $LaMnO_3$: A neutron-scattering study, Phys. Rev. B **54**, 15149 (1996).

[24] G. Chaboussant, A. Sieber, S. Ochsenbein, H.-U. Güdel, M. Murrie, A. Honecker, N. Fukushima, and B. Normand, Exchange interactions and high-energy spin states in Mn_{12}-acetate, Phys. Rev. B **70**, 104422 (2004).

[25] X. Fabrèges, I. Mirebeau, S. Petit, P. Bonville, and A. A. Belik, Frustration-driven magnetic order in hexagonal $InMnO_3$, Phys. Rev. B **84**, 054455 (2011).

[26] S. Mandal, A. Andreanov, Y. Crespo, and N. Seriani, Incommensurate helical spin ground states on the hollandite lattice, Phys. Rev. B **90**, 104420 (2014).

[27] M. F. Lapa and C. L. Henley, Ground states of the classical antiferromagnet on the pyrochlore lattice, arXiv:1210.6810; J.-B. Fouet, M. Mambrini, P. Sindzingre, and C. Lhuillier, Planar pyrochlore: A valence-bond crystal, Phys. Rev. B **67**, 054411 (2003); Y. Iqbal, T. Müller, P. Ghosh, M. J. P. Gingras, H. O. Jeschke, S. Rachel, J. Reuther, and R. Thomale, Quantum and Classical Phases of the Pyrochlore Heisenberg Model with Competing Interactions, Phys. Rev. X **9**, 011005 (2019).

[28] A. M. Larson, P. Moetakef, K. Gaskell, C. M. Brown, G. King, and E. E. Rodriguez, Inducing ferrimagnetism in insulating hollandite $Ba_{1.2}Mn_8O_{16}$, Chem. Mater. **27**, 515 (2015).

[29] J. M. Luttinger and L. Tisza, Theory of dipole interaction in crystals, Phys. Rev. **70**, 954 (1946); J. M. Luttinger, A note on the ground state in antiferromagnetics, *ibid.* **81**, 1015 (1951); T. A. Kaplan and N. Menyuk, Spin ordering in three-dimensional crystals with strong competing exchange interactions, Philos. Mag. **87**, 3711 (2007); P. Ghosh, T. Müller, F. P. Toldin, J. Richter, R. Narayanan, R. Thomale, J. Reuther, and Y. Iqbal, Quantum paramagnetism and helimagnetic orders in the Heisenberg model on the body centered cubic lattice, Phys. Rev. B **100**, 014420 (2019).

[30] P. A. McClarty, O. Sikora, R. Moessner, K. Penc, F. Pollmann, and N. Shannon, Chain-based order and quantum spin liquids in dipolar spin ice, Phys. Rev. B **92**, 094418 (2015).

[31] P. Balla, Y. Iqbal, and K. Penc, Degenerate manifolds, helimagnets, and multi-Q chiral phases in the classical Heisenberg antiferromagnet on the face-centered-cubic lattice, Phys. Rev. Research **2**, 043278 (2020).

[32] K. Millard and H. S. Leff, Infinite-spin limit of the quantum Heisenberg model, J. Math. Phys. **12**, 1000 (1971).

[33] E. H. Lieb, The classical limit of quantum spin systems, Commun. Math. Phys. **31**, 327 (1973).

[34] I. Kimchi and A. Vishwanath, Kitaev-Heisenberg models for iridates on the triangular, hyperkagome, kagome, fcc, and pyrochlore lattices, Phys. Rev. B **89**, 014414 (2014).

[35] E. F. Bertaut, Configurations magnétiques méthode de fourier, J. Phys. Chem. Solids **21**, 256 (1961).

[36] Z. Nussinov, Commensurate and incommensurate $O(n)$ spin systems: Novel even-odd effects, a generalized Mermin-Wagner-Coleman theorem, and ground states, arXiv:cond-mat/0105253.

[37] P. C. Hohenberg, Existence of long-range order in one and two dimensions, Phys. Rev. **158**, 383 (1967); N. D. Mermin and H. Wagner, Absence of Ferromagnetism or Antiferromagnetism in One- or Two-Dimensional Isotropic Heisenberg Models, Phys. Rev. Lett. **17**, 1133 (1966).

[38] S. W. Lovesey, *Theory of Neutron Scattering from Condensed Matter* (Clarendon, Oxford, UK, 1984).

[39] J. Villain, R. Bidaux, J.-P. Carton, and R. Conte, Order as an effect of disorder, J. Phys. II (France) **41**, 1263 (1980).

[40] E. F. Shender, Antiferromagnetic garnets with fluctuationally interacting sublattices, Zh. Eksp. Teor. Fiz. **83**, 326 (1982) [JETP **56**, 178 (1982)].

[41] T. Holstein and H. Primakoff, Field dependence of the intrinsic domain magnetization of a ferromagnet, Phys. Rev. **58**, 1098 (1940).

[42] U. Hizi and C. L. Henley, Anharmonic ground state selection in the pyrochlore antiferromagnet, Phys. Rev. B **80**, 014407 (2009).

[43] T. Niwa and K. Motizuki, Magnon lifetime and its effect on magnon sideband in MnO, J. Phys. Soc. Jpn. **41**, 1224 (1976).

[44] K. Majumdar and T. Datta, Non-linear spin wave theory results for the frustrated $S = \frac{1}{2}$ Heisenberg antiferromagnet on a body-centered cubic lattice, J. Phys.: Condens. Matter **21**, 406004 (2009).

[45] S. A. Owerre, Two-dimensional Dirac nodal loop magnons in collinear antiferromagnets, J. Phys.: Condens. Matter **30**, 28LT01 (2018).

[46] P. Balla, Y. Iqbal, and K. Penc, Affine lattice construction of spiral surfaces in frustrated Heisenberg models, Phys. Rev. B **100**, 140402(R) (2019).

[47] C. L. Henley, Ordering Due to Disorder in a Frustrated Vector Antiferromagnet, Phys. Rev. Lett. **62**, 2056 (1989).

[48] H. Kawamura, Spin-wave analysis of the antiferromagnetic plane rotator model on the triangular lattice-symmetry breaking in a magnetic field, J. Phys. Soc. Jpn. **53**, 2452 (1984).

[49] L. O. Manuel, M. I. Micheletti, A. E. Trumper, and H. A. Ceccatto, Heisenberg model on the $\frac{1}{5}$-depleted square lattice and the CaV_4O_9 compound, Phys. Rev. B **58**, 8490 (1998).

[50] R. L. Doretto, Plaquette valence-bond solid in the square-lattice J_1-J_2 antiferromagnet Heisenberg model: A bond operator approach, Phys. Rev. B **89**, 104415 (2014).

[51] S. Sachdev and R. N. Bhatt, Bond-operator representation of quantum spins: Mean-field theory of frustrated quantum Heisenberg antiferromagnets, Phys. Rev. B **41**, 9323 (1990).

[52] R. R. P. Singh, Z. Weihong, C. J. Hamer, and J. Oitmaa, Dimer order with striped correlations in the J_1-J_2 Heisenberg model, Phys. Rev. B **60**, 7278 (1999).

[53] V. N. Kotov, J. Oitmaa, O. P. Sushkov, and Z. Weihong, Low-energy singlet and triplet excitations in the spin-liquid phase of the two-dimensional J_1-J_2 model, Phys. Rev. B **60**, 14613 (1999).

[54] M. E. Zhitomirsky and K. Ueda, Valence-bond crystal phase of a frustrated spin-1/2 square-lattice antiferromagnet, Phys. Rev. B **54**, 9007 (1996).

[55] B. Kumar, Bond operators and triplon analysis for spin-S dimer antiferromagnets, Phys. Rev. B **82**, 054404 (2010).

[56] P. Ghosh, A. K. Verma, and B. Kumar, Plaquette-triplon analysis of magnetic disorder and order in a trimerized spin-1 kagome Heisenberg antiferromagnet, Phys. Rev. B **93**, 014427 (2016).

[57] P. Ghosh and B. Kumar, Spontaneous dimerization and moment formation in the Hida model of the spin-1 kagome antiferromagnet, Phys. Rev. B **97**, 014413 (2018).

[58] P. Ghosh, Y. Iqbal, T. Müller, R. T. Ponnaganti, R. Thomale, R. Narayanan, J. Reuther, M. J. P. Gingras, and H. O. Jeschke, Breathing chromium spinels: A showcase for a variety of pyrochlore Heisenberg Hamiltonians, npj Quantum Mater. **4**, 63 (2019).

[59] T. Lugan, L. D. C. Jaubert, and A. Ralko, Topological nematic spin liquid on the square kagome lattice, Phys. Rev. Res. **1**, 033147 (2019).

[60] H. Nakano and T. Sakai, The two-dimensional S=1/2 Heisenberg antiferromagnet on the *Shuriken* lattice a lattice composed of vertex-sharing triangles, J. Phys. Soc. Jpn. **82**, 083709 (2013).

[61] I. Rousochatzakis, R. Moessner, and J. van den Brink, Frustrated magnetism and resonating valence bond physics in two-dimensional kagome-like magnets, Phys. Rev. B **88**, 195109 (2013).

[62] K. Morita and T. Tohyama, Magnetic phase diagrams and magnetization plateaus of the Spin-1/2 antiferromagnetic Heisenberg model on a square-kagome lattice with three nonequivalent exchange interactions, J. Phys. Soc. Jpn. **87**, 043704 (2018).

[63] J. Richter, J. Schulenburg, P. Tomczak, and D. Schmalfuß, Topological nematic spin liquid on the square kagome lattice, Condens. Matter Phys. **12**, 507 (2009).

[64] A. Ralko and I. Rousochatzakis, Resonating-Valence-Bond Physics is Not Always Governed by the Shortest Tunneling Loops, Phys. Rev. Lett. **115**, 167202 (2015).

[65] P. W. Anderson, Ordering and antiferromagnetism in ferrites, Phys. Rev. **102**, 1008 (1956).

[66] J. Reuther and P. Wölfle, J_1-J_2 frustrated two-dimensional Heisenberg model: Random phase approximation and functional renormalization group, Phys. Rev. B **81**, 144410 (2010).

[67] Y. Iqbal, R. Thomale, F. P. Toldin, S. Rachel, and J. Reuther, Functional renormalization group for three-dimensional quantum magnetism, Phys. Rev. B **94**, 140408(R) (2016).

[68] L. Capriotti, F. Becca, A. Parola, and S. Sorella, Resonating Valence Bond Wave Functions for Strongly Frustrated Spin Systems, Phys. Rev. Lett. **87**, 097201 (2001).

[69] W.-J. Hu, F. Becca, A. Parola, and S. Sorella, Direct evidence for a gapless Z_2 spin liquid by frustrating Néel antiferromagnetism, Phys. Rev. B **88**, 060402(R) (2013).

[70] Y. Iqbal, T. Müller, H. O. Jeschke, R. Thomale, and J. Reuther, Stability of the spiral spin liquid in $MnSc_2S_4$, Phys. Rev. B **98**, 064427 (2018).

[71] S. Chillal, Y. Iqbal, H. O. Jeschke, J. A. Rodriguez-Rivera, R. Bewley, P. Manuel, D. Khalyavin, P. Steffens, R. Thomale, A. T. M. Nazmul Islam, J. Reuther, and B. Lake, Evidence for a three-dimensional quantum spin liquid in $PbCuTe_2O_6$, Nat. Commun. **11**, 2348 (2020).

[72] G. Baskaran, G. Santhosh, and R. Shankar, Exact quantum spin liquids with Fermi surfaces in spin-half models, arXiv:0908.1614.

[73] X.-G. Wen, Quantum orders and symmetric spin liquids, Phys. Rev. B **65**, 165113 (2002).

[74] M. Hering, J. Sonnenschein, Y. Iqbal, and J. Reuther, Characterization of quantum spin liquids and their spinon band structures via functional renormalization, Phys. Rev. B **99**, 100405(R) (2019).

[75] Y. Iqbal, F. Becca, and D. Poilblanc, Projected wave function study of $\mathbb{Z}_2$ spin liquids on the kagome lattice for the spin-$\frac{1}{2}$ quantum Heisenberg antiferromagnet, Phys. Rev. B **84**, 020407(R) (2011).

[76] Y. Iqbal, F. Becca, S. Sorella, and D. Poilblanc, Gapless spin-liquid phase in the kagome spin-$\frac{1}{2}$ Heisenberg antiferromagnet, Phys. Rev. B **87**, 060405(R) (2013).

[77] Y. Iqbal, D. Poilblanc, and F. Becca, Vanishing spin gap in a competing spin-liquid phase in the kagome Heisenberg antiferromagnet, Phys. Rev. B **89**, 020407(R) (2014).

[78] Y. Iqbal, D. Poilblanc, and F. Becca, Spin-$\frac{1}{2}$ Heisenberg J_1-J_2 antiferromagnet on the kagome lattice, Phys. Rev. B **91**, 020402(R) (2015).

[79] Y. Iqbal, W.-J. Hu, R. Thomale, D. Poilblanc, and F. Becca, Spin liquid nature in the Heisenberg J_1-J_2 triangular antiferromagnet, Phys. Rev. B **93**, 144411 (2016).

[80] Y. Iqbal, D. Poilblanc, R. Thomale, and F. Becca, Persistence of the gapless spin liquid in the breathing kagome Heisenberg antiferromagnet, Phys. Rev. B **97**, 115127 (2018).

[81] Y. Iqbal, F. Becca, and D. Poilblanc, Valence-bond crystal in the extended kagome spin-$\frac{1}{2}$ quantum Heisenberg antiferromagnet: A variational monte carlo approach, Phys. Rev. B **83**, 100404(R) (2011).

[82] Y. Iqbal, F. Becca, and D. Poilblanc, Valence-bond crystals in the kagomé spin-1/2 Heisenberg antiferromagnet: a symmetry classification and projected wave function study, New J. Phys. **14**, 115031 (2012).

[83] N. Shannon, T. Momoi, and P. Sindzingre, Nematic Order in Square Lattice Frustrated Ferromagnets, Phys. Rev. Lett. **96**, 027213 (2006).

[84] Y. Iqbal, P. Ghosh, R. Narayanan, B. Kumar, J. Reuther, and R. Thomale, Intertwined nematic orders in a frustrated ferromagnet, Phys. Rev. B **94**, 224403 (2016).

[85] M. E. Zhitomirsky, Octupolar ordering of classical kagome antiferromagnets in two and three dimensions, Phys. Rev. B **78**, 094423 (2008).